Mixing in density- and viscosity-stratified flows

Cite as: Phys. Fluids **34**, 096605 (2022); https://doi.org/10.1063/5.0108337
Submitted: 08 July 2022 • Accepted: 24 August 2022 • Accepted Manuscript Online: 25 August 2022 • Published Online: 20 September 2022
Published open access through an agreement with JISC Collections

P. A. Allen, R. M. Dorrell, O. G. Harlen, et al.

Physics of Fluids ARTICLE scitation.org/journal/phf

Mixing in density- and viscosity-stratified flows

Cite as: Phys. Fluids **34**, 096605 (2022); doi: 10.1063/5.0108337
Submitted: 8 July 2022 · Accepted: 24 August 2022 ·
Published Online: 20 September 2022

View Online Export Citation CrossMark

P. A. Allen,[1,a)] R. M. Dorrell,[2] O. G. Harlen,[1] R. E. Thomas,[2] and W. D. McCaffrey[3]

AFFILIATIONS

[1]School of Mathematics, Faculty of Engineering and Physical Sciences, University of Leeds, Leeds LS2 9JT, United Kingdom
[2]Energy and Environment Institute, University of Hull, Hull HU6 7RX, United Kingdom
[3]School of Earth and Environment, Faculty of Environment, University of Leeds, Leeds LS2 9JT, United Kingdom

[a)]Author to whom correspondence should be addressed: matpaa@leeds.ac.uk

ABSTRACT

The lock-exchange problem is used extensively to study the flow dynamics of density-driven flows, such as gravity currents, and as a canonical problem to mixing in stratified flows. Opposite halves of a domain are filled with two fluids of different densities and held in place by a lock-gate. Upon release, the density difference drives the flow causing the fluids to slosh back and forth. In many scenarios, density stratification will also impose a viscosity stratification (e.g., if there are suspended sediments or the two fluids are distinct). However, numerical models often neglect variable viscosity. This paper characterizes the effect of both density and viscosity stratification in the lock-exchange configuration. The governing Navier–Stokes equations are solved using direct numerical simulation. Three regimes are identified in terms of the viscosity ratio $\mu_2/\mu_1 = (1+\gamma)$ between the dense and less dense fluids: when $\gamma \ll 1$, the flow dynamics are similar to the equal-viscosity case; for intermediate values ($\gamma \sim 1$), viscosity inhibits interface-scale mixing leading to a global reduction in mixing and enhanced transfer between potential and kinetic energy. Increasing the excess viscosity ratio further ($\gamma \gg 1$) results in significant viscous dissipation. Although many gravity or turbidity current models assume constant viscosity, our results demonstrate that viscosity stratification can only be neglected when $\gamma \ll 1$. The initial turbidity current composition could enhance its ability to become self-sustaining or accelerating at intermediate excess viscosity ratios. Currents with initially high excess viscosity ratio may be unable to dilute and propagate long distances because of the decreased mixing rates and increased dissipation.

I. INTRODUCTION

Gravity currents are flows driven by pressure gradients resulting from density differences. These may be the result of temperature, suspended sediment, or solute differences.[1] Gravity currents form significant geophysical flows in atmospheric, terrestrial, and subaqueous environments. Examples include turbidity currents, pyroclastic currents, sea-breeze fronts, or the spreading of industrial effluent in rivers and oceans.[2] Dilution of these flows through mixing with the ambient affects the dynamics of propagation by reducing the driving density difference, increasing flow thickness, and through the effective drag of accelerating entrained fluid,[3] which can significantly impact the run-out time and length scales of these flows. Gravity currents have been extensively studied by theoretical and experimental approaches, often based around the idealized lock-exchange or lock-release problem, where dense fluid is released by the rapid removal of a gate, providing a well-controlled initial condition. In this paper, the lock-exchange problem refers explicitly to the case where the dense and ambient fluid each occupies one-half of the domain. Upon release, a pair of gravity currents are created as the dense fluid is driven into the lighter ambient and vice versa. This method provides a suitable means to create repeatable fixed-volume gravity currents that allow meaningful comparison to analytical models.[4–8]

The form of a gravity current is characterized by the Reynolds number of the flow $Re = UL/\nu$, where L and U are suitable length and velocity scales and ν is the kinematic viscosity. The Reynolds number is the ratio between inertial and viscous forces, and when $Re \gg 1$, the flow evolves under a balance between buoyancy and inertial forces.[9] Gravity currents with $Re \gtrsim 10^4$ exhibit similar turbulent dynamics.[10] Surface tension effects can become important for flows involving (nearly) immiscible fluids. The Bond number $Bo = g'L^2/\sigma$, where g' is the reduced gravity and σ is the surface tension, is the ratio between surface tension and buoyancy forces. For small-scale flows, when $Bo < 1$, surface tension becomes significant.[1] In general, mixing or entrainment rates in gravity currents are a function of all relevant dimensionless groups of the flow and proportional to the velocity between the current and the ambient.[11,12] For miscible fluids, the

Schmidt number $Sc = \nu/D$ is the ratio between momentum ν and mass D diffusivities and depends only on material properties. Large Schmidt numbers indicate the mass diffusivity is negligible compared with the vorticity. As the limit tends to infinity, this corresponds to immiscible fluids that can only be mixed at macroscopic scales through interface instability and fluid turbulence.[13] In the context of gravity currents, initial studies suggested a Schmidt number Sc similarity for values larger than roughly 1 (Ref. 14) or that the influence of the Schmidt number Sc is quite small in the range 0.2–5.[15] Bonometti and Balachandar[13] demonstrated that quantitative changes between gravity currents with high or low Schmidt numbers Sc are observed, but the influence on structure dynamics is weak for $Re > 10^4$.

Two significant types of underwater gravity currents are sub-aqueous debris flows and turbidity currents. Both have a density difference with the surrounding water caused by the presence of suspended sediment and are the dominant process for transporting sediment from shallow to deep water environments.[16] Turbidity currents can cause significant damage to pipelines, oil rig moorings,[17,18] and seafloor telecommunication cables,[19,20] and their deposits (turbidites) form some of the largest hydrocarbon reservoirs.[21] Turbidity currents have low sediment concentration and exhibit Newtonian behavior, and the sediment is suspended by fluid turbulence.[16] By contrast, debris flows have high sediment concentration and sediment is suspended by particle–particle interactions. Further, sub-aqueous debris flows can exhibit non-Newtonian behavior, such as non-zero yield strength and shear-thinning or shear-thickening, which is enhanced with the presence of cohesive material like clay.[22] Debris flows and turbidity currents are end members of a spectrum of sub-aqueous sediment-laden gravity-driven flows. Sub-aqueous debris flows can mix with the surrounding water and transform into turbidity currents through a variety of mechanisms discussed in Felix and Peakall.[23] For particulate flows of mono-dispersed spheres, local concentrations of suspended material affect the rheology of flows leading concentration-dependent viscosity and non-Newtonian affects at higher concentrations. Approximately, a linear relationship is observed between concentration and viscosity at low concentrations (up to 20%).[24] However, most turbidity current simulations assume Newtonian rheology and constant viscosity.[25] Flows can transform from high to low concentration[23] or from the low to high concentration[26] through a variety of mechanisms. Initial flow composition is a key control on whether or not these flows transform[23,27] and often either limited mixing or a cascade of mixing is observed as the viscosity of the current decreases with increased mixing.

Recent experimental lock-release studies extend the configuration to non-rectangular cross sections,[28] currents that propagate over rough surfaces[29] or obstacles[30–32] and in unconfined settings.[33] Experimental studies have also explored the pulsed flows generated from a multiple lock-release.[34–36] Theoretical models calculate the position of the gravity current head using dimensional arguments or integral models and a balance between the buoyancy force and either inertial or viscous forces.[6,37] Depth-averaged models have also been used extensively to study gravity current motion.[3,38–40] With the increase in available computational power, depth-resolved models have been increasingly used to study turbulent gravity currents over the past 20 years.[16] These models fall into three categories: Reynolds-averaged Navier–Stokes (RANS) equations; large-eddy simulations (LES); and direct numerical simulation (DNS). RANS models require closure with the supplementation of empirical models and parameterize the turbulent structures within the flow, for example, two-equation RANS models such as k–ε[41,42] or k–ω.[43] Large-eddy simulations (LES) resolve the large-scale turbulent structures, but are supplemented with empirical, sub-grid-scale models to parameterize the small-scale turbulent motions below a cutoff length scale.[44] However, in the context of stratified mixing, Özgökmen *et al.*[45] demonstrate that mixing rates vary with sub-grid-scale model, and the best fit to DNS is dependent on the Reynolds number. DNS requires no parametrization and numerically integrates the Navier–Stokes equations directly. Härtel *et al.*[46] produced some of the first DNS of a gravity current in the lock-exchange configuration. The Navier–Stokes equations were solved using a mixed spectral/spectral-element method (SEM) discussed and were validated by Härtel *et al.*[47] For a particle-driven flow, Necker *et al.*[14,48] used the method of Härtel *et al.*,[46,47] which included particle deposition and entrainment, but neglects viscosity variations. Özgökmen *et al.*[45] extend their previous testing of large-eddy simulation (LES) of the lock-exchange problem[49,50] with DNS conducted with spectral-element solver NEK5000. DNS using pseudo-spectral methods for a longer domain has also been conducted.[51,52] The smallest turbulent length scale of the flow to be resolved is the Kolmogorov length scale l_b, which gives a computational cost proportional to Re^3 for DNS. However, for miscible fluids, the diffusive or Batchelor length scale $l_\nu = Sc^{1/2} l_b$ is the smallest length scale to be resolved when $Sc > 1$. This gives a more restrictive computational cost of $Sc^2 Re^3$ as discussed by Meiburg *et al.*[25]

This paper explores the dynamics of a gravity driven flow where a density and viscosity stratification exists in a lock-exchange configuration. The configuration used replicates that of Özgökmen *et al.*,[45] which was used to study stratified mixing of equal-viscosity Boussinesq fluids. In the region of flow where mixing occurs, the density and viscosity depend on the local concentration of the denser fluid. The Navier–Stokes equations are solved using the spectral element solver NEK5000.[53] To the best of our knowledge, the work presented here is the first DNS study of a gravity driven flow in the lock-exchange configuration with both a viscosity and a density stratification. We demonstrate that three distinct regimes exist based on the excess viscosity ratio γ between the denser and less dense fluid. The rates of mixing, energy transfer between potential and kinetic, and propagation speed change in each regime. At lowest excess viscosity ratios, assuming constant viscosity is reasonable. However, for $\gamma \sim 1$ or $\gamma \gg 1$, the viscosity contrast changes the flow dynamics relative to the equal viscosity case and constant viscosity cannot be assumed. This has implications to gravity-driven flows with viscosity contrasts and their modeling as viscosity contrasts can enhance run-out lengths or inhibit flow transformation. This paper is structured as follows: details of the numerical model and a description of the cases conducted are presented in the methodology Sec. II; results are presented in Sec. III; implications are discussed in Sec. IV; and finally, we conclude in Sec. V.

II. METHODOLOGY

A. Fluid dynamics equations

A gravity-driven flow of two miscible fluids of different densities and viscosities in a lock-exchange configuration is modeled with the Navier–Stokes equations and single transport equation for the local phase concentration of denser fluid, ϕ. The denser fluid, which forms

an intruding gravity current along the base, is denoted as fluid 2 and the lighter or ambient fluid as fluid 1. Each pure phase has constant density ρ_i and dynamic viscosity μ_i. The phase concentration $\phi \in [0,1]$ represents the concentration of fluid 2, and thus, $\phi = 1$ or $\phi = 0$ corresponds to points of purely fluids 2 or 1, respectively. This is an adaptation of the volume-of-fluid (VOF) method,[54] as here the viscosity is also a function of the phase concentration.

For variable viscosity fluids, Moresi *et al.*[55] demonstrated that the accuracy of two finite-element-type schemes depends on the viscosity gradients between adjacent cells rather than the contrast across the entire domain. Therefore, to maximize the range of global viscosity contrasts in this study, linear relationships are assumed for both viscosity and density

$$\rho(\phi) = \phi\rho_2 + (1-\phi)\rho_1 = \left(1 + \frac{\rho_2 - \rho_1}{\rho_1}\phi\right)\rho_1, \tag{1}$$

$$\mu(\phi) = \mu^*(\phi)\mu_1 = (1+\gamma\phi)\mu_1, \tag{2}$$

where $\gamma = (\mu_2 - \mu_1)/\mu_1$, the excess viscosity ratio, is a constant. The Boussinesq lock-exchange problem is a canonical example of symmetrical flow dynamics. Adding a viscosity variation into the problem breaks this symmetry as the viscous dissipation and hence momentum in each fluid will be different.

The domain Ω used is a rectilinear box, in three spatial dimensions (x, y, z), of length L, height H, and width, W, Fig. 1. Thus, $\Omega = \{(x,y,z) \in \mathbb{R}^3 | x \in [-L/2, L/2], y \in [0,H], z \in [0,W]\}$. The aspect ratio L/H is an important parameter of the system. When $L \gg H$, the flow is essentially a two-layer exchange flow with counter-propagating gravity currents with the appearance of Kelvin–Helmholtz rolls.[56] Mixing occurs predominately by turbulent breakdown and second instabilities about these rolls in a stably stratified setting.[45] In a short domain with $L < H$, the gravity currents would rapidly encounter the $x = \pm L/2$ boundaries. Here, an aspect ratio $L/H = 2$ is chosen to provide regions of the flow when stably stratified mixing occurs and more complex convection-driven mixing at the $x = \pm L/2$ boundaries. A longer domain, for example, $L/H = 5$ used by Özgökmen *et al.*,[50] would increase the computational cost and limit the range of excess viscosity ratios γ studied. As the goal of this paper was to study a large range of γ the value of $L/H = 2$ largest feasible. The width aspect ratio W/H is fixed at 1, which is the same as the

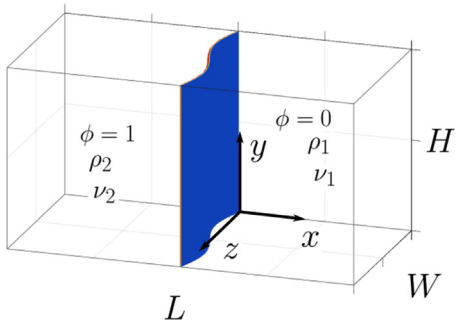

FIG. 1. Geometry for the lock-exchange problem. A box length L, height H, and width W in the x, y, and z directions, respectively. The aspect ratios used in all simulations are $L/H = 2$ and $W/H = 1$.

studies of Özgökmen *et al.*[45,50] and similar to value of 1.5 used by Härtel *et al.*[46] and Cantero *et al.*[51] A value less than one might inhibit the size of the largest turbulent structures that form within the flow.

It is assumed that the flow is isothermal and the Bond number Bo is sufficiently large so that surface tension and other intermolecular forces are neglected.[1] Further, the density difference between the two layers is assumed to be small, $\rho_2/\rho_1 \sim 1$, so that the Boussinesq approximation[57] can be applied. This neglects density variations in all terms that are not multiplied by gravitational acceleration g. The Boussinesq approximation is valid for density ratios up to 1.1 or even 1.2 for gravity currents as the transition from Boussinesq to non-Boussinesq regimes is not dramatic.[9,13] For the spatial coordinates $\mathbf{x} = (x,y,z)$ and time t, the dimensionless Navier–Stokes equations for an incompressible Boussinesq fluid are as follows (Tritton):[58]

$$\frac{D\mathbf{u}}{Dt} = -\nabla p + \frac{1}{Re_1}\nabla\cdot\boldsymbol{\tau} - \frac{\phi}{Fr}(0,-1,0), \tag{3}$$

$$\nabla\cdot\mathbf{u} = 0, \tag{4}$$

where $\mathbf{u}(\mathbf{x},t) = (u(\mathbf{x},t), v(\mathbf{x},t), w(\mathbf{x},t))$ is the velocity along the three spatial axes, $Re_1 = HU/\nu_1 = \rho_1 HU/\mu_1$ is the fluid 1 Reynolds number, and $Fr = U^2/g'H$ is the Froude number, where $g' = g(\rho_2 - \rho_1)/\rho_1$ is the reduced gravity. The stress tensor, $\boldsymbol{\tau}$, is expressed as

$$\boldsymbol{\tau} = \mu^*(\phi)\left[(\nabla\mathbf{u}) + (\nabla\mathbf{u})^T\right]. \tag{5}$$

The length scale H, velocity scale, $U = \sqrt{g'H/2}$, and the advective timescale H/U were the dimensional scales used to non-dimensionalize the problem. This yields $Fr = U^2/g'H = 1/2$ and the dimensionless domain $\Omega = \{(x,y,z) \in \mathbb{R}^3 | x \in [-1,1], y \in [0,1], z \in [0,1]\}$. The transport of fluid 2 phase concentration ϕ is modeled with an advection–diffusion equation

$$\frac{D\phi}{Dt} = \nabla\cdot\left(\frac{1}{Re_1 Sc_1}\nabla\phi\right), \tag{6}$$

where $Sc_1 = \nu_1/D_m$ is the fluid 1 Schmidt number and D_m is the mass diffusivity, which is a constant determined by the fluid 1 kinematic viscosity $\nu_1 = \mu_1/\rho_1$. Three dimensionless parameters categorize the flow behavior: the ambient Reynolds number Re_1, the excess viscosity ratio γ, and the fluid 1 Schmidt number Sc_1. For flows with Schmidt number $Sc > 1$, the Batchelor length scale l_b determines the smallest scale within the flow[25] and is the scale at which fluctuations in concentration can exist before diffusion becomes dominant.[25] To ensure the choice of Schmidt number has limited effect on the flow dynamics, the constant value $Sc_1 = 7$ is chosen. This produces a mass diffusivity of $D_m = \nu_1/7$. For variable viscosity calculation, the mixture Schmidt number Sc is not constant throughout the domain and takes value $Sc = 7(1+\gamma\phi) \geq 7$. Crucially, the mixture Schmidt number remains in the similarity regime $Sc > 1$. The overall computational cost is not expected to increase by the variable mixture Schmidt number Sc, because Sc increases linearly with viscosity, Re decreases linearly, and computation cost is $O(Sc^2 Re^3)$. However, as discussed earlier, large viscosity differences may require a more resolved solution to capture the gradients in viscosity that arise near the fluid 1/fluid 2 interface. In Appendix A, it is demonstrated that this value of the fluid 1 Schmidt number Sc_1 is sufficiently large for the total integration time $T_{\text{int}} = 13.5$ chosen here using the mixing metrics defined in Secs. II D

and II E. Significantly longer integration times would see a large contribution to mixing from diffusion.

The velocity is set to zero everywhere initially, $\mathbf{u}(x, y, z, 0) = \mathbf{0}$. The boundaries of the domains at $x = -1, x = 1, y = 0, y = 1$ are prescribed as free-slip or symmetry planes

$$\begin{aligned} \mathbf{u}(-1, y, z, t) \cdot \mathbf{n} = 0, \quad \mathbf{u}(1, y, z, t) \cdot \mathbf{n} = 0, \\ \mathbf{u}(x, 0, z, t) \cdot \mathbf{n} = 0, \quad \mathbf{u}(x, 1, z, t) \cdot \mathbf{n} = 0, \end{aligned} \tag{7}$$

where $\mathbf{n}$ is the outward pointing normal on the domain boundary $\partial\Omega$. At the $z = 0$ and $z = 1$ planes, a periodic condition is imposed

$$\begin{aligned} \mathbf{u}(x, y, 0, t) = \mathbf{u}(x, y, 1, t), \\ \phi(x, y, 0, t) = \phi(x, y, 1, t). \end{aligned} \tag{8}$$

The initial conditions consist of a concentration profile, Fig. 1, in which the majority of the fluid is either at $\phi = 0$ or $\phi = 1$. A small sinusoidal perturbation is introduced to the interface in the z direction $\eta(z) = 0.05 \sin(2\pi z)$, and the sharp jump between $\phi = 0$ and $\phi = 1$ is replaced by a linear variation in concentration over a small region of width $2\zeta_0 = 0.01$

$$\phi(x, y, z, 0) = \begin{cases} 1 & \text{if} \quad x \in [-1, -\zeta_0 - \eta(z)], \\ \dfrac{1}{2\zeta_0}(\zeta_0 - x - \eta(z)) & \text{if} \quad x \in [-\zeta_0 - \eta(z), \zeta_0 - \eta(z)], \\ 0 & \text{if} \quad x \in [\zeta_0 - \eta(z), 1]. \end{cases} \tag{9}$$

This sinusoidal perturbation was introduced during previous DNS studies of the lock-exchange problem because two-dimensional initial conditions did not develop span-wise asymmetries during much of the simulation.[45,50] The boundary conditions remove the viscous boundary layers that would require significantly more computational resources. In the context of gravity currents, a no-slip boundary condition along the bottom boundary results in the nose of the gravity current rising up from the bed and forcing ambient fluid underneath as it propagates. This leads to entrainment into the body of the current. With a free-slip boundary condition (7), the propagating wavefront will not rise up from the boundary, and hence, no fluid will be entrained through this mixing mechanism. A no-slip boundary condition would require a significant increase in resolution near the boundaries leading to increased computational cost. Numerous studies use simplified boundary conditions to allow better resolution of the mixing dynamics that occur, for example, free-slip conditions on the $y = \pm 1$ boundaries and $x = \pm 1$ boundaries of the domain and periodic boundary conditions in the cross-stream direction.[45,46,50,51] Further studies have been conducted in a two-dimensional domain, but these cannot capture any three-dimensional variations in the flow.

B. Cases conducted

For the set of simulations conducted, the fluid 1, or ambient, Reynolds number Re_1 is fixed at 1000. By varying the coefficient γ, the fluid 2 Reynolds number defined as $Re_2 = Re_1/(1 + \gamma)$ is varied. Six different values of γ are chosen for the simulations conducted, $\gamma = 0, 0.1, 1, 2, 4, 10$. The corresponding dimensionless numbers for each case are presented in Table I. The equal-viscosity or base case ($\gamma = 0$) has the Reynolds numbers in each layer equal and provides a source of comparison to the other cases. The largest value of γ that is feasible in this study is $\gamma = 10$. The remaining cases vary the viscosity difference over two orders of magnitude between $\gamma = 10$ and the base case, $\gamma = 0$. The total integration time for each case T_{int} is fixed at 13.5 in dimensionless units. As discussed by Özgökmen *et al.*,[45] this corresponds to 3.35 times the time for the current to cross one length of the domain and 2.15 times the buoyancy period. Thus, although it is not sufficient for the flow to come to rest, it enables multiple sloshing to be captured and is sufficient for the bulk of turbulent mixing to occur.[45] The sloshing period is defined as the time between subsequent maxima of potential energy (PE), which corresponds to half the buoyancy period.

TABLE I. Fluid 2 Re_2 and fluid 1 Re_1 Reynolds numbers, and fluid 1 Schmidt numbers Sc_1 corresponding to the six values of excess viscosity ratio γ studied.

γ	Re_2	Re_1	Sc_1
0	1000	1000	7
0.1	910	1000	7
1	500	1000	7
2	333	1000	7
4	200	1000	7
10	91	1000	7

C. Solver and numerical details

The Navier–Stokes and advection–diffusion equations (3)–(6) are solved using the numerical code NEK5000,[53] which is based on spectral element methods (SEM).[59] SEM are a class of high-order weighted residual techniques and a subset of finite-element methods (FEM).[60] In this computational method, the domain is split into E rectilinear elements with basis functions formed from an $(\mathcal{N} - 1)$ th order tensor product polynomial in each spatial direction. Thus, there are $\mathcal{N}^3$ degrees of freedom for each element E. Spectral element methods are optimized for polynomial orders $(\mathcal{N} - 1)$ between 7 and 15 and exhibit exponential convergence in space.[59]

A regular mesh is created by setting the number of elements in each spatial direction (N_x, N_y, N_z). This gives the total number of elements $\mathcal{E} = N_x N_y N_z$. Each element e then contains $\mathcal{N}^3$ nodes corresponding to relative positions of the Gauss–Lobatto–Legendre (GLL) points when the element is mapped onto the reference cube. The time-stepping for the system of equations follows the $\mathbb{P}_{\mathcal{N}} - \mathbb{P}_{\mathcal{N}}$ approach presented in Tomboulides *et al.*[61,62] For the equal-viscosity case ($\gamma = 0$), the stress tensor is contracted to $\tau = \mu\nabla^2\mathbf{u}$ by using the incompressibility condition, which reduces the computational cost.

For convection-dominated flows, the Galerkin formulation suffers from a well-known instability arising from under-resolved boundary layers, for example, Brown.[63] Filtering is introduced to address this instability and involves multiplying the highest order basis polynomial coefficient by a factor $1 - \beta_f$. A value $\beta_f = 0.05$ is used throughout our simulations, which is consistent with other studies in the literature.[45,64–66] High-frequency oscillations can also lead to instability through an aliasing error[67] that arises from the non-linear terms in the Navier–Stokes equations. To correct for this, $\lceil 3(\mathcal{N} + 1)/2 \rceil$ GLL points are used in each direction for the integration of the non-linear term, where $\lceil\ \rceil$ is the ceiling or round-up function. This is similar to 3/2-rule in pseudo-spectral methods.[68] Solver tolerances are expressed

in terms of residual error and set to 10^{-5} for the pressure solver and 10^{-7} for the Helmholtz solvers (velocity and scalar-transport equations). The tolerances are as large as possible to minimize the computational time without affecting the accuracy solution. NEK5000 has been extensively validated against experimental data for a variety of fluid dynamic problems including flow through rod bundles[69] and T-junctions,[70] parallel jets,[66] buoyancy-driven cavity flows,[71] and others.[72] The results presented here for the equal viscosity case ($\gamma = 0$) were verified against those of Özgökmen *et al.*[45]

D. Residual potential energy (RPE) and energy balance

Upon release, the potential energy stored in the initial distribution of fluid 2 is converted into kinetic energy (KE) as it is driven horizontally by the density difference. When the propagating wavefront of dense fluid reaches the $x = 1$ boundary, it is driven vertically converting some of the kinetic energy back into potential energy. The potential energy is then converted back into kinetic energy as the density difference drives the flow back the other way. The total kinetic energy $KE(t)$ and potential energy $PE(t)$ are given functions of time[73]

$$KE(t) = \frac{1}{2}\int_\Omega (u^2 + v^2 + w^2)\,\mathrm{d}V, \tag{10}$$

$$PE(t) = \int_\Omega 2\phi y\,\mathrm{d}V. \tag{11}$$

As a result of the Boussinesq approximation, only the potential energy PE contains the excess density ϕ. The total energy of the system at time t therefore satisfies

$$KE(t) + PE(t) + D_v(t) = PE(0) = 1, \tag{12}$$

where $D_v(t)$ is the energy converted into heat by viscous dissipation. Thus, by calculating the kinetic energy KE and potential energy PE over time, the total viscous dissipation over time is obtained from

$$D_v(t) = 1 - PE(t) - KE(t). \tag{13}$$

The potential energy $PE(t)$ is decomposed into two components: residual potential energy (RPE) and available potential energy (APE). The residual potential energy over time $RPE(t)$ provides a measure for quantifying the mixing that occurs within a closed system.[73] At fixed time t, $RPE(t)$ represents the minimum potential energy that is obtained through adiabatic redistribution of the fluid within the domain to a stratified state with the most dense fluid at the bottom and there is no density variation across the length or width of the flow. $RPE(t)$ is monotonically increasing and is energy irreversibly lost to mixing. The available potential energy $APE(t) = PE(t) - RPE(t)$ is the maximum amount of potential energy that is available to be converted into kinetic energy $KE(t)$.[74] The total energy in the system is expressed as

$$1 = KE(t) + RPE(t) + APE(t) + D_v(t). \tag{14}$$

The dense phase concentration ϕ is equivalent to the excess density in the system (3)–(6) and is used to determine the RPE following the method of Tseng and Ferziger.[75] The normalized residual potential energy $NRPE(t)$ is defined as

$$NRPE(t) = \frac{RPE(t) - RPE(0)}{RPE_{\max} - RPE(0)}, \tag{15}$$

where $RPE_{\max} = 1$. This provides a mixing metric $NRPE(t) \in [0, 1]$ with 0 and 1 corresponding to no mixing and fully mixed, respectively, and is distinct from the definition of Winters *et al.*[73] who instead define

$$NRPE(t) = \frac{RPE(t) - RPE(0)}{RPE(0)}. \tag{16}$$

However, as $2RPE(0) \approx RPE_{\max}$ with the initial conditions (9), both methods give similar results, but the definition (15) is more applicable to a study mixing with a wider range of initial conditions.

E. Mixing volume fraction

A second measure of mixing, based on the volume fraction of the domain in which some mixing has occurred, is also used to characterize the rate of mixing. For a parameter β_v, the volume fraction in the domain that is within concentration $[\beta_v, 1 - \beta_v]$ is

$$\theta(t; \beta_v) = \frac{1}{2}\int_\Omega \mathcal{F}(\phi; \beta_v)\,\mathrm{d}V, \tag{17}$$

where $\mathcal{F}(\phi; \beta_v)$ is the box filter function defined as

$$\mathcal{F}(\phi; \beta_v) = \begin{cases} 1 & \text{if} \quad \phi \in [\beta_v, 1 - \beta_v], \\ 0 & \text{otherwise.} \end{cases} \tag{18}$$

This method is similar to that of Bonometti and Balachandar.[13] However, they normalize the integral by a volume based on the depth H and the distance the protruding wavefronts have traveled. In this study, the flow reaches the $x = \pm 1$ boundaries within a fraction of the total integral time T and so the total volume 2 is used instead. The parameter β_v is set to 0.01. Similarly to the residual potential energy, the mixing volume fraction $\theta(t)$ is scaled using its initial $\theta(0)$ and maximum, $\theta_{\max} = 1$, value

$$N\theta(t) = \frac{\theta(t) - \theta(0)}{\theta_{\max} - \theta(0)} \tag{19}$$

to provide a metric between 0 and 1 with the values $N\theta(t) = 0$ and $N\theta(t) = 1$ corresponding, respectively, to no mixing of the initial state and to mixing having occurred everywhere (i.e., $\phi \in [\beta, 1 - \beta]$, $\forall (x, y, z) \in \Omega$). The statistics $N\theta$ and normalized residual potential energy $NRPE$ provide two different methods for evaluating the amount of mixing that has occurred in the flow. For sharp initial conditions, that is, ϕ only taking values 0 or 1, $N\theta(t) \geq NRPE(t)$, with equality only if $\phi(x, y, z, t) \in \{0, 0.5, 1\}\ \forall (x, y, z) \in \Omega$. With the linear concentration gradient over a region of thickness $2\zeta_0 = 0.01$, it is possible for $N\theta(t) < NRPE(t)$. However, the difference would be close to zero.

Normalized mixing volume $N\theta$ provides a more global picture of the mixing, whereas $NRPE$ includes effects from local mixing across concentration gradients. For example, if a small amount of diffusion occurs and convection redistributes changes in concentration ϕ over the domain, so that a relatively sharp transition is maintained, but most regions of the flow have concentration $\phi \in [\beta, 1 - \beta]$, then $N\theta$ will increase rapidly compared with $NRPE$. Conversely, if the interface itself is smoothed, but the majority of the flow has not mixed, then $NRPE$ will increase at a rate similar to $N\theta$. Thus, distinctions between the rates that $N\theta$ and $NRPE$ increase are used to indicate the relative

importance of local mixing near the interface when comparing different cases.

III. RESULTS

In this section, the results from all cases are reported on mesh C for $\gamma = 0, 0.1, 1$ and E for $\gamma = 2, 4, 10$. These meshes are detailed in a resolution study conducted in Appendix B and consist of 5.4×10^4 and 1.5×10^5 elements, respectively. Further, every simulation is conducted with a Courant number Cr of 0.1.

Pseudo-color plots of fluid 2 concentration ϕ on the center-plane $z = 1/2$ at $\Delta t = 0.5$ time intervals are displayed in Fig. 2 (Multimedia view) for the equal-viscosity case ($\gamma = 0$). The plane is colored by concentration ϕ with $\phi = 1$ corresponding to a deep red and $\phi = 0$ corresponding to deep blue. Intermediate values are colored from red to white to blue as concentration decreases, thus highlighting regions of the flow that have mixed. Over the first few time-steps, a symmetric profile of concentration is observed as the density difference drives fluid 2 to the right ($x > 0$) and fluid 1 to the left ($x < 0$). Just before the wavefronts hit the $x = \pm 1$ boundaries, Kelvin–Helmholtz-like rolls start to form behind the propagating wavefronts. These rolls remain sharply defined, with little mixing, until they are absorbed by the reflecting wavefronts after $t = 4.5$. After this, the rate of mixing increases and a large mixed region is observed behind each wavefront. After $t = 8.5$, the wavefronts are no longer clearly defined because of the increase in mixing and dissipation within the flow. Toward the end of the simulation, only a thin region near $y = 0$ and $y = 1$ remains completely unmixed. The symmetry of the flow is maintained throughout. This is to be expected due to the equal viscosities of the two fluids.

At nine different time-steps, pseudo-color plots of concentration are presented for excess viscosity ratios $\gamma = 1$ and $\gamma = 10$ in Fig. 3 (Multimedia view). At $t = 1$, the flows appear similar, but by $t = 2$, the increasing viscosity in the basal layer inhibits the formation of the Kelvin–Helmholtz rolls. For the intermediate case ($\gamma = 1$), Kelvin–Helmholtz rolls are still produced, but less fluid is exchanged between the bulk of each layer. The Kelvin–Helmholtz rolls entrain more fluid in $x > 0$ than the corresponding roll in $x < 0$ for $\gamma = 1$. The returning wavefront in $x < 0$ for $\gamma = 10$ appears in a similar shape to $\gamma = 0$ and $\gamma = 1$ without the Kelvin–Helmholtz roll. A region of thicker transition between fluids in $\gamma = 10$ indicates that shear-induced

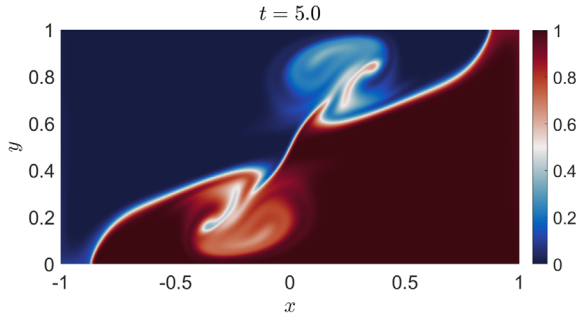

FIG. 2. Pseudo-color plots of concentration ϕ on the center plane $z = 1/2$ over $t = 0.5$ time-steps for the equal-viscosity case ($\gamma = 0$). At $t = 5$, the reflected wavefronts are shown. Deep red corresponds to the denser fluid 2, and deep blue corresponds to less dense fluid 1. Multimedia view: https://doi.org/10.1063/5.0108337.1

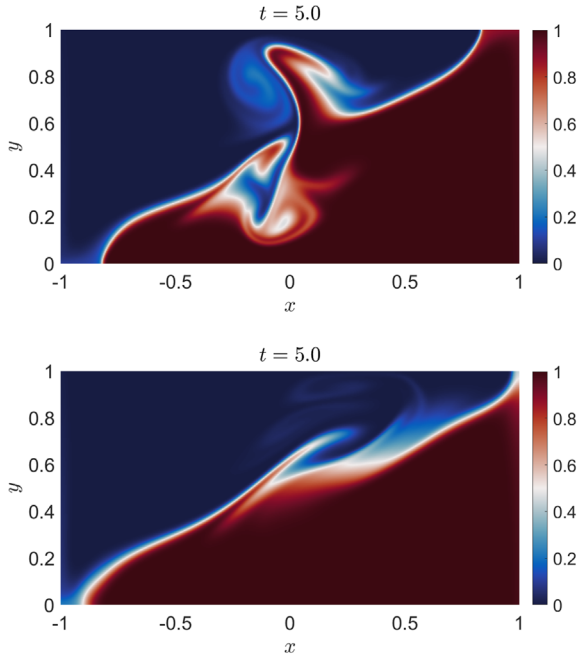

FIG. 3. Pseudo-color plots of concentration ϕ on the center plane $z = 1/2$ for two different cases: $\gamma = 1$ (top) and $\gamma = 10$ (bottom). At $t = 5$, the reflected wavefronts are shown. Deep red corresponds to the denser fluid 2, and deep blue corresponds to less dense fluid 1. Multimedia views: https://doi.org/10.1063/5.0108337.2; https://doi.org/10.1063/5.0108337.3

mixing has still occurred. However, less overall mixing occurs. As the simulation time increases toward $t = 13.5$, more unmixed regions are observed as the fluid 2 viscosity increases. Further, the sloshing periods increase when the excess viscosity ratio γ is equal to 1 because there is significantly more dense in $x > 0$ when compared to the equal-viscosity case. Conversely, there is less dense fluid in $x < 0$ for $\gamma = 10$ when compared to the equal-viscosity case indicating a decrease in the sloshing period.

To visualize the full three-dimensional variation in the concentration ϕ, isosurface plots are displayed for cases $\gamma = 0$ and $\gamma = 10$ in Fig. 4 (Multimedia view) at different time-steps. At $t = 3.5$, the wavefronts are reflecting off the $x = \pm 1$ boundary. Isosurfaces are surfaces of constant concentration ($\phi = 0.05, 0.25, 0.5, 0.75, 0.95$ for these cases). Each of the five surfaces is colored from blue to green to red with increasing fluid 2 concentration. The Kelvin–Helmholtz rolls observed in the equal-viscosity case $\gamma = 0$ extend over the entire cross-stream (z direction) of the flow. However, after the reflected wavefronts cross at $t = 5.5$, the flow is more chaotic. The cross-stream variation of the extreme isosurfaces ($\phi = 0.05$ and $\phi = 0.95$) extend over much of the domain by $t = 9.5$ for $\gamma = 0$. By contrast, $\gamma = 10$ shows only slight cross-stream variation through to $t = 9.5$, signifying the effect of increasing viscosity on the flow. However, from $t = 2.5$ onward, the variation in the flow across $\phi = 0.5$ is apparent with the formation of a smaller Kelvin–Helmholtz roll only in fluid 1. The sinusoidal initial conditions (9) lead to the creation of large vortices that occupy $z < 1/2$ and $z > 1/2$ regions. These are the largest turbulent structures observed in the domain. For small values of γ, these break

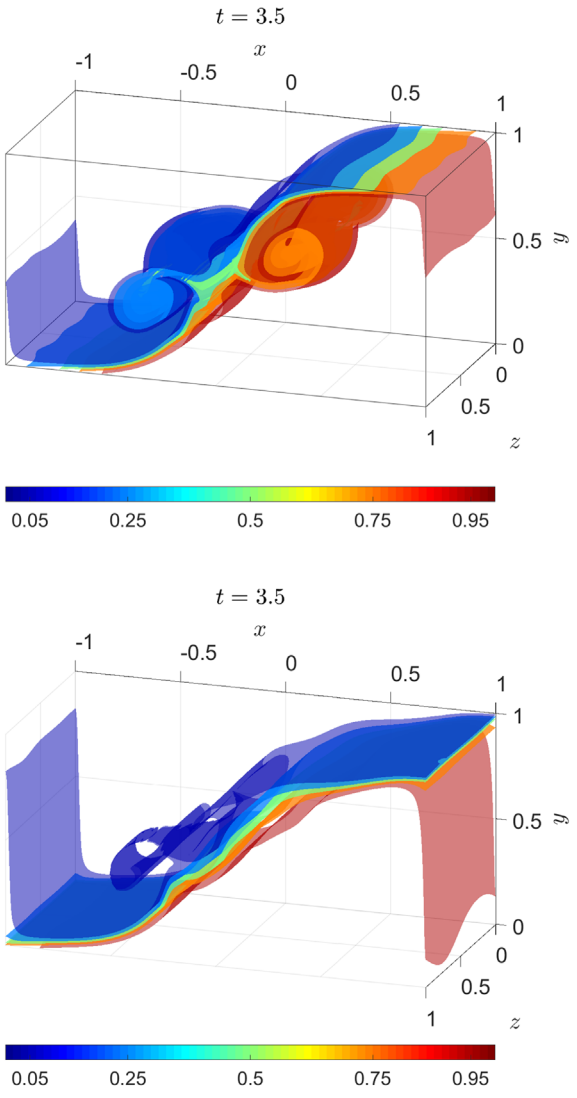

FIG. 4. Isosurface plots of concentration ϕ for $\gamma = 0$ (top) and $\gamma = 10$ (bottom) cases. Each colored surface corresponds to concentrations $\phi = (0.05, 0.25, 0.5, 0.75, 0.95)$ ranging from blue ($\phi = 0.05$) to red ($\phi = 0.95$). At $t = 3.5$, the wavefronts are reflecting from the $x = \pm 1$ boundaries. Multimedia views: https://doi.org/10.1063/5.0108337.4; https://doi.org/10.1063/5.0108337.5

up into smaller vortices by the integration time $T = 13.5$ in both dense and less dense fluids. When the excess viscosity ratio is large $\gamma \gg 1$, the smaller vortices are suppressed by viscosity in the denser fluid.

A. Mixing and energy distribution

Normalized residual potential energy *NRPE* and normalized-mixing fraction $N\theta$ are displayed against time in Fig. 5 for all cases. Both mixing metrics show that mixing rates decrease as fluid 2 viscosity increases. The cases with $\gamma = 0$, $\gamma = 0.1$, and $\gamma = 1$ all exhibit similar levels of mixing up to $t = 6$ for *NRPE*, and up to $t = 9$ for $N\theta$. Increasing the excess viscosity ratio to $\gamma = 2$ and $\gamma = 4$ reduces the rate of increase in *NRPE* after $t = 2$. However, the normalized mixing fraction $N\theta$ remains similar to the lower excess viscosity ratio values for $\gamma = 2$ and $\gamma = 4$ until $t = 8$ and $t = 5$, respectively. Thus, the initial impact of increasing the viscosity is to reduce the local mixing at the sharp concentration gradient. This then leads to a reduction in global mixing. The reduction in interface-scale mixing is clearly observed in center-plane plots in Figs. 2 (Multimedia view) and 3 (Multimedia view). At $t = 5$, the wavefronts have reflected off the $x = \pm 1$ boundaries and so dense fluid (red) is moving to the left and less dense fluid (blue) is moving to the right in Figs. 2 and 3.

In Fig. 6, potential energy *PE*, kinetic energy *KE*, available potential energy *APE*, and energy dissipated by viscosity D_v are plotted against time for the cases $\gamma = 0, 0.1, 1, 2, 4, 10$. An exchange between potential and kinetic energy is observed as the flow sloshes back and forth. The maxima of potential energy coincide with the wavefronts reflecting off the $x = \pm 1$ boundaries and, as expected, the kinetic energy minima. Conversely, the potential energy minima coincide with kinetic energy maxima. As the flow sloshes back and forth, the viscosity of the flow dissipates energy reducing the magnitude of the maxima. Larger fluid 2 viscosities increase the rate that energy is dissipated initially, and for all cases, the rate of dissipation increases sharply during the periods when kinetic energy is at its largest. The period of oscillation, measured as the time between peaks or troughs, varies slightly with excess viscosity ratio γ and is very close to 4, the estimated period for the flow as discussed by Özgökmen.[45]

Up until $t = 6$, the $\gamma = 1$ and $\gamma = 2$ cases exhibit similar behavior to the equal-viscosity case $\gamma = 0$. However, after $t = 6$, two key differences can be observed: first, the minima and maxima of potential energy *PE* and kinetic energy *KE* are smaller and larger, respectively; second, the time between the extrema increases. Thus, more of the available potential energy *APE* is converted to kinetic energy *KE* and vice versa. As the excess viscosity ratio increases further, $\gamma = 4$ and $\gamma = 10$, the extra dissipation reduces the total energy in the system, and hence, the maxima of potential energy *PE* and kinetic energy *KE* are also lower than the equal-viscosity case. Conversely, the exchange between potential energy *PE* and kinetic energy *KE* occurs more quickly after $t = 6$, with $\gamma = 4$ having a sloshing period similar to the equal-viscosity case and $\gamma = 10$ a reduced period. These changing speeds are consistent with the center-plane concentration profiles in Figs. 2 (Multimedia view) and 3 (Multimedia view). At $t = 13.5$, the $\gamma = 10$ case has moved past the lowest potential energy state with more dense fluid in $x < 0$. For $\gamma = 0$ and $\gamma = 1$, the fluid has yet to reach the lowest potential energy state. For $\gamma = 1$, there is a significant amount of fluid remaining in $x > 0$.

To explore the energy loss from the system further, the change in *RPE* over time D_m is introduced

$$D_m(t) = RPE(t) - RPE(0). \tag{20}$$

This measures the total energy that has been irretrievably lost to mixing from the initial state and is equal to $(RPE_{\max} - RPE(0))NRPE$. The change in *RPE* over time D_m, total viscous dissipation D_v, and the rate of change of both quantities over time, $\mathrm{d}D_m/\mathrm{d}t$ and $\mathrm{d}D_v/\mathrm{d}t$, is presented in Fig. 7. The gradients of D_m and D_v are calculated using a forward-difference scheme and a total of 200 points equally spaced points obtained by interpolating the piece-wise cubic spline for D_m and D_v. At $t = 0$, these gradients are assumed to be 0. As expected, all cases exhibit local maxima of viscous dissipation rate when the kinetic

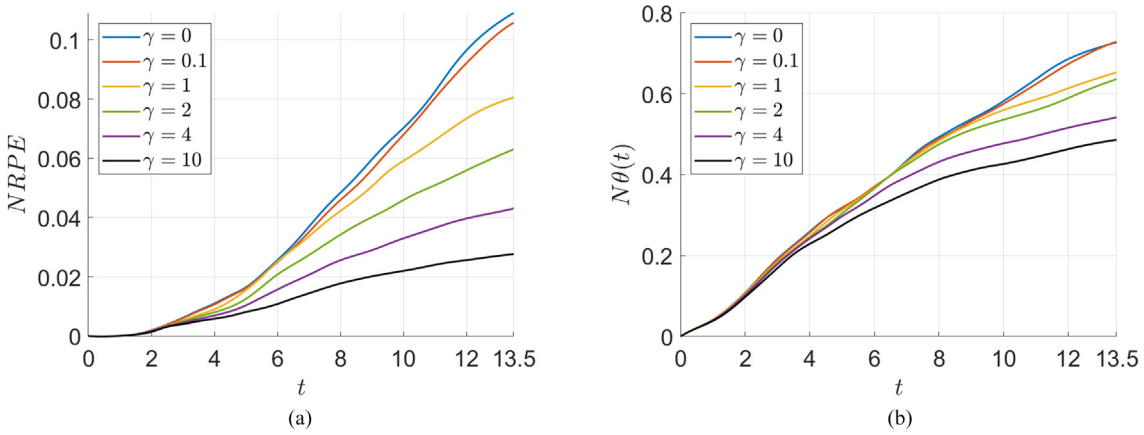

FIG. 5. Normalized residual potential energy *NRPE* (a) and normalized-θ $N\theta$ (b) for the cases $\gamma = 0, 0.1, 1, 2, 4, 10$.

energy is largest. Initially, the rate of mixing is similar for all cases. A global maximum is reached during the simulation. The time this global maximum occurs reduces as the fluid 2 viscosity is increased. Further, the rate of viscous dissipation $\gamma = 10$, although initially taking the largest values, decreases at a rate much faster than the other cases and has slower rates of viscous diffusion at the extrema near $t = 9$ and $t = 11.5$. After the first period of sloshing, the equal-viscosity case ($\gamma = 0$) and the lowest excess viscosity case ($\gamma = 0.1$) no longer exhibit the smooth behavior in the rate of change of viscous dissipation $\mathrm{d}D_v/\mathrm{d}t$ when compared to the other cases. A possible explanation for this is that larger and more energetic turbulent structures form in these two cases, which can significantly affect the fluid 2 concentration on a global scale,

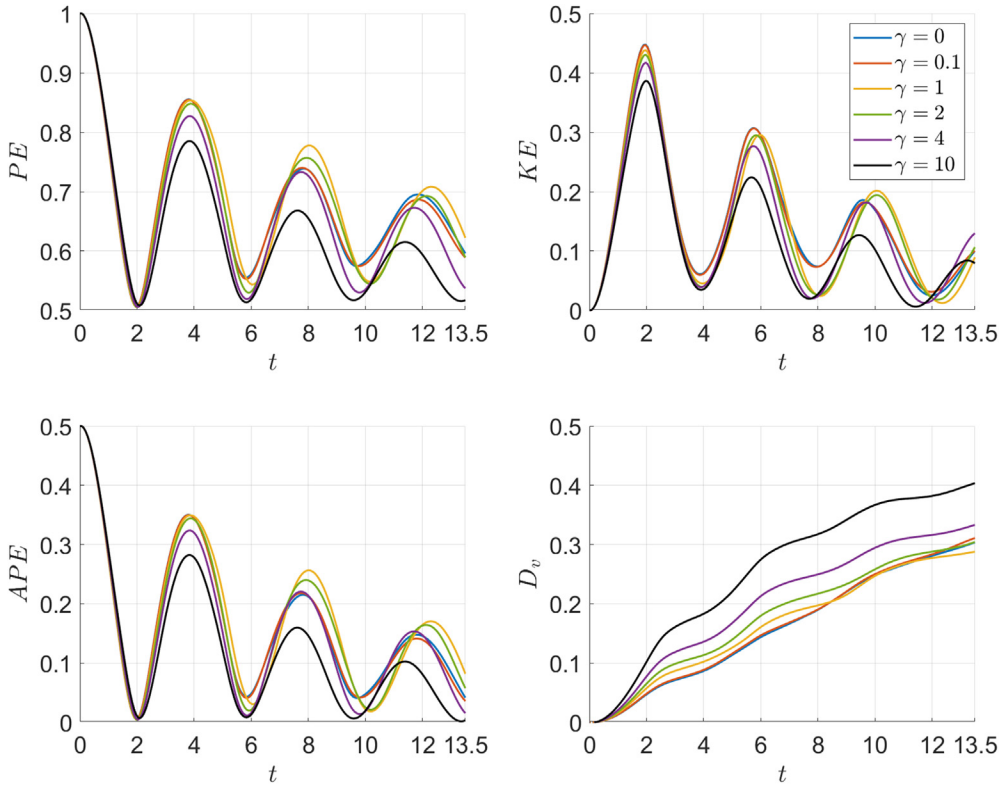

FIG. 6. Energy distributions for the cases $\gamma = 0, 0.1, 1, 2, 4, 10$: potential energy *PE* (top-left), kinetic energy *KE* (top-right), available potential energy *APE* (bottom-left), and energy dissipated by viscosity D_v (bottom-right).

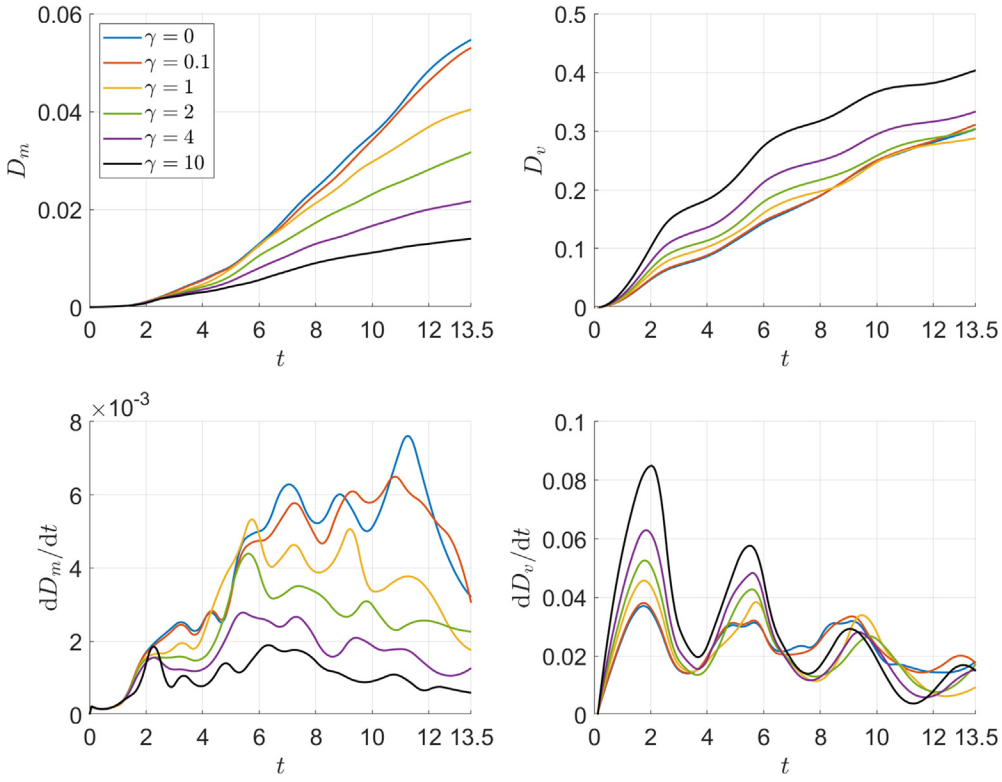

FIG. 7. For the cases $\gamma = 0, 0.1, 1, 2, 4, 10$: Gain in residual potential energy $D_m = RPE(t) - RPE(0)$ (top-left); energy lost to viscous dissipation D_v (top-right); rate of change of residual potential energy dD_m/dt (bottom-left); and the rate of change of viscous dissipation dD_v/dt (bottom-right).

which perturbs the flow away from a simple sloshing back and forwards that would be obtained in a non-Boussinesq system. The most dissipative flow ($\gamma = 10$) has $D_v = 0.4$ at the integration time $T = 13.5$. Using the properties of water for the less dense fluid and a density ratio of 1.1, this corresponds to a temperature increase in $\Delta T \sim 2 \times 10^{-8\circ} C$ confirming our isothermal assumption. The irreversible form of mixing efficiency $Ri_g^* = D_m/(D_m + D_v)$ is the fraction of energy lost in the flow that has contributed to mixing.[76] For lock-release flows, Ri_g^* has been calculated to be 0.12 or 0.13 for saline-driven flows released into water[76,77] for large Reynolds numbers based on the head speed U_f, $Re_f = \rho U_f H/2\mu > 3 \times 10^3$. The mixing efficiency drops sharply when $Re_f < 3000$. The mixing efficiency Ri_g^* for the flows considered in this paper increases from 0.035 5 ($\gamma = 10$) to 0.153 ($\gamma = 0$). For $\gamma \ll 1$, the simulations predict the flows mix more efficiently than the lock-release experiments. This could be a result of the free-slip boundary conditions imposed as this would reduce the energy lost to viscous dissipation at the flow boundaries. However, for gravity currents, a no-slip boundary can drive fluid underneath the propagating head and lead to increase entrainment and hence mixing rates. Using high-resolution experimental measurements, Mukherjee and Balasubramanian[77] demonstrate that regions of high mixing efficiency occur after large dissipative stirring events such as vortical overturns near the interface. Both Mukherjee and Balasubramanian[77] and Agrawal *et al.*[76] use a long domain ($L \gg H$), and the flows do no interact with the end walls. Therefore, the larger overturns generated when the wave fronts reflect of the end walls likely add to the mixing efficiency in our case.

Isosurface plots of the concentrations for excess viscosity ratio $\gamma = 1$ are presented in Fig. 8 (Multimedia view). Comparing with Fig. 4 (Multimedia view), at $t = 6$ the wavefronts have just reflected off the $x = \pm 1$ boundaries with the denser fluid 2 traveling back toward the right ($x > 0$) and fluid 1 toward the left. These wavefronts reflect back off the $x = \pm 1$ boundaries and cross again just before $t = 9$. At $t = 6$, apart from the phase difference identified in the energy plots Fig. 6, the flows look similar for $\gamma = 0$ and $\gamma = 1$. By $t = 9$, substantially more mixing has occurred in the equal-viscosity case $\gamma = 0$ with the isosurfaces spanning a larger area of the domain Ω. The viscosity contrast in the $\gamma = 1$ case stabilizes the flow and produces more structured and smoother isosurfaces. This is seen when compared to the equal-viscosity case ($\gamma = 0$) at $t = 9$, where the $\phi = 0.25, 0.5, 0.75$ isosurfaces are relatively well defined even when the flow is folding in on itself. For $\gamma = 10$ and at $t = 6$, the free surface deformation is significantly reduced. By $t = 9$, the mixing in $\gamma = 0$ affects the majority of the flow and all isosurfaces are more distorted. In $\gamma = 1$ and $\gamma = 10$, the isosurfaces remain closer together indicating less mixing across the fluid interface. The $\phi = 0.05$ isosurface for $\gamma = 1$ is significantly more broken up near $x = 1$ compared with the $\phi = 0.95$ isosurface near $x = -1$. This highlights asymmetry in the flow and demonstrates that the increased viscosity in fluid 2 is inhibiting the mixing into that fluid.

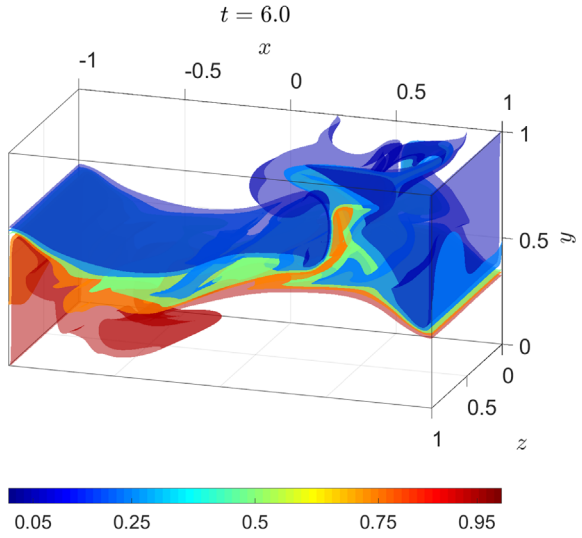

FIG. 8. Isosurface plots of concentration ϕ for excess viscosity ratio $\gamma = 1$. Each colored surface corresponds to concentrations $\phi = (0.05, 0.25, 0.5, 0.75, 0.95)$ ranging from deep blue ($\phi = 0.05$) to deep red ($\phi = 0.95$). At $t = 6$, the wavefronts are about to reflect for the second time off the $x = \pm 1$ boundaries. Multimedia view: https://doi.org/10.1063/5.0108337.6

The surface area of the $\phi = 0.5$ isosurface $A_{0.5}(t)$ represents the size of the fluids 1 and 2 interface. Initially, the interface surface area increases in size as the flow spreads out laterally, Fig. 9. After $t = 2$, a decrease in surface area is observed for all cases except $\gamma = 1$. This corresponds to the wavefronts reflecting off the $x = \pm 1$ boundaries and the flows becoming more horizontally stratified. For $\gamma = 1$, however, the decrease is negligible. All cases, except for $\gamma = 10$, exhibit a sharp increase in surface area $A_{0.5}(t)$ again between $t = 4$ and $t = 5.5$, and in particular, $\gamma = 2$ and $\gamma = 4$ produce similar results to the equal-viscosity case before $t = 5.5$. However, after $t = 6$, $\gamma = 4$ transitions into behavior similar to the higher viscosity case. This suggests that during the first three sloshing periods, the fluid 2 viscosity increase predominantly affects the surface-destruction rather than surface-creation mechanisms. Flow shear leads to surface creation within the flow. Interface-scale mixing and diffusion then reduce it. Oscillatory behavior is observed with local maxima of $A_{0.5}(t)$ coinciding with kinetic energy maxima. This corresponds to when the wavefronts cross and the flow is in the lowest potential energy state. The $\gamma = 1$ case exhibits the largest surface area between $t = 3$ and $t = 11$ before rapidly decreasing at the end of the flow. The $\gamma = 10$ case still exhibits the sharp increase in interface size as the flow spreads horizontally from release, but decays in an oscillatory behavior thereafter. Viscosity affects the flow during the first few time units by dissipating the energy required for significant interface deformation.

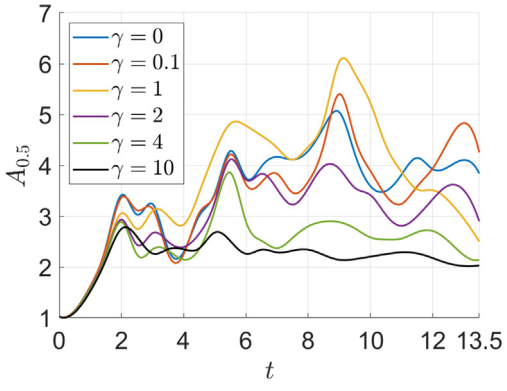

FIG. 9. Surface area of the $\phi = 0.5$ isosurface $A_{0.5}$ against time for the cases $\gamma = 0, 0.1, 1, 2, 4, 10$.

The cases with $\gamma = 1$ and $\gamma = 2$ appear as intermediary cases in which the increase in fluid 2 viscosity is not large enough to inhibit the shear and interface creation on the system scale, but is sufficient to inhibit local interface-scale mixing. The increase in maximum available potential energy *APE* for $\gamma = 1$ and $\gamma = 2$ at $t = 8$ and $t = 12$ arises because of the decreased mixing in the flow. This is aided by the increased viscosity. The magnitude of these local maxima is smaller for $\gamma = 2$, and as γ is further increased, dissipation results in a decreasing trend in the maximum values at $t = 8$ and $t = 12$.

IV. DISCUSSION AND IMPLICATIONS

In this section, implications of our work are discussed in the context of the real-world density- and viscosity-stratified flows presented in the introduction. Three different regimes are identified based on the excess viscosity ratio γ: When $\gamma \ll 1$, the fluids 1 and 2 viscosities are similar, and therefore, the viscosity gradient across the interface is small. In this regime, the dynamics are comparable to the equal-viscosity case, and therefore, neglecting a viscosity stratification would be a reasonable approximation. When $\gamma \sim 1$, the viscosity contrast stabilizes the interface enabling more potential energy to be converted to kinetic energy, and vice versa, as the flow sloshed back and forth. This is most prevalent in our simulations when $\gamma = 1$, where the local minima and maxima of kinetic and potential energy are smaller and larger, respectively, than the equal-viscosity case after two sloshing periods $t > 8$, Fig. 6. Initially, more viscous dissipation occurs for both $\gamma = 1$ and $\gamma = 2$ compared with the equal-viscosity case. However, total viscous dissipation is less than the equal viscosity case by the end of the simulation. Viscosity plays a key role in limiting interface deformation and suppressing turbulence, which leads to a reduction in the total mixing that occurs within the flow, Fig. 5, and an increase in the period of sloshing, Fig. 6. The enhanced ability of the flow to transfer energy between potential energy and kinetic energy, and the reduction to mixing rates and total energy dissipated may lead to gravity currents with $\gamma \sim 1$ having an enhanced run-out length and an increase to associated hazards. In particular, unconfined or partially confined turbidity currents flowing down a slope have access to an (almost) limitless supply of potential energy and can become self-accelerating.[78] In the $\gamma \sim 1$ regime, viscosity stratification significantly affects the flow dynamics, and neglecting the viscosity contrast is difficult to justify. In the third regime, $\gamma \gg 1$, a large viscosity gradient exists across the interface, and the amount of mixing is further reduced compared to $\gamma \sim 1$, which enhances the interface preservation. In particular, for $\gamma = 4$, the extrema in kinetic and potential energy are similar to the equal-viscosity case, despite greater viscous dissipation. Thus, enhanced energy transfer mechanisms discussed for $\gamma \sim 1$ are still present. However, viscous dissipation increases significantly as the excess viscosity ratio increases, and in particular, for $\gamma = 10$, nearly 40% of

the initial energy is dissipated by viscosity during the integration time, Fig. 6. The sloshing period decreases for these high-viscosity contrast flows.

In many physical contexts, variable density will naturally impose a viscosity contrast. For example, saline solutions of water and sodium chloride can impose a density ratio of up to 1.2, but a viscosity ratio as large as 1.7. Similarly, at a fixed concentration of 25 g/kg, varying the temperature between 50 °C and 20 °C increases the density by 0.6%, but the viscosity by 75%.[79,80] The viscosity differences can be orders of magnitude different for similar densities. Glycerol is extensively used in the food and pharmaceutical industries[81] and as a mixture with water to produce Newtonian fluids over a wide range of viscosities to use in experimental studies of gravity currents.[82] These glycerol/water mixtures can have viscosity ratios as large as $\sim O(10^3)$, but with a maximum density difference of 25%.[83] Most numerical studies of gravity currents with a density difference caused by miscible fluids, suspension of sediment, or a dissolved solute neglect variations in viscosity.[45,46,50,84–86] In some cases, this is implicitly assumed, for example, Ouillon *et al.*[87] and Steenhauer *et al.*[88] This approximation is useful as it enables simplification of the stress term in the Navier–Stokes equations and reduces computational cost.[13] However, this can be only motivated in the $\gamma \ll 1$ regime.

Many rheological models exist for the suspension of rigid spheres and are reviewed by Shewan and Stokes.[89] These models express the ratio of the mixture to interstitial viscosity as a function of the phase concentration by volume c. Note that this is distinct from the mass volume fraction as the density of particles can be significantly larger than the interstitial liquid. For example, Sumner *et al.*[26] used silica sand with a density of 2448 kg/m^3 in the study of transitional turbidity currents and debris flows. Provided the particles are non-colloidal and the flows are Newtonian, these can be used a rheological models for turbidity currents.[90] The presence of clays or other colloidal particles add non-Newtonian effects cannot be captured by these models. For rigid spheres, the mixture rheology remains Newtonian up to relatively large concentrations of about $c = 0.5$. At low phase concentrations c, the rheology is approximately linear as obtained with the theoretical result of Einstein[91]

$$\mu_2 = \mu_1(1 + 2.5c). \tag{21}$$

This equation is no longer valid as the phase concentration increases and particle–particle interactions become significant. At larger phase concentrations ($c > 0.2$), Maron and Pierce[92] developed a model that can be used to predict the viscosity of mixtures up to the maximum packing fraction c_m,

$$\mu_2 = \mu_1\left(1 - \frac{c}{c_m}\right)^{-2}. \tag{22}$$

The maximum packing fraction c_m theoretically takes the value $c_m = 0.64$ for rigid mono-dispersed spheres. For poly-dispersed spheres, maximum packing fraction c_m is dependent on the particle size distribution and experimentally measured values are generally between 0.6 and 0.8.[89] A similar model to the Maron and Pierce model is that of Krieger and Dougherty.[93] This may fit to experimental data more accurately as it has an additional fitting parameter, but the difference between the two is within experimental error and the model of Krieger and Dougherty[93] under predicts the mixture viscosity at concentrations close to maximum packing.[89] Using the Maron and Pierce model,[22] three different regimes of particle suspensions are identified: Low phase concentrations ($c \sim 0.04$) produce an excess viscosity ratio $\gamma \sim 0.1$ using with either Maron and Pierce or Einstein's relation; at intermediate concentration ($c \sim 0.18$), the Maron and Pierce model produces values between $\gamma \sim 0.66$ and $\gamma \sim 1.04$ depending on the maximum packing fraction c_m; at high concentrations ($c = 0.4$), the viscosity contrast is large with values of excess viscosity ratio γ between 3 and 8. These particle concentrations reflect the three regimes of excess viscosity ratio γ identified earlier in this section.

Similar to a viscosity contrast, gravity currents with non-Boussinesq density stratification in a lock-exchange configuration no longer produce symmetric solutions and a backward traveling shock can arise in the body of the denser fluid.[9] Further, the denser head propagates faster and dissipates more energy, whereas the less dense head remains similar to a Boussinesq case for two-dimensional gravity currents.[15] In a DNS study of non-Boussinesq lock-exchange gravity currents Birman *et al.*,[15] the kinematic viscosity $\nu = \mu/\rho$ is kept fixed, while both the dynamic viscosity and density are increased in the denser current. Qualitatively similar results are obtained if the dynamic viscosity is fixed and the kinematic viscosity is varied. Our results demonstrate that fixing the density and increasing kinematic and dynamic viscosities also leads to an increased propagation speed and dissipation for $\gamma \gg 1$. For a solid phase density of 2448 mg/m^3, the density ratios of these three regimes are 1.06, 1.26, and 1.58, respectively. However, the transition between the Boussinesq and non-Boussinesq regime is not dramatic, and so the regime limit can be set to a density ratio of 1.1, or even 1.2 for gravity currents.[9,13] Therefore, when discussing implications for turbidity currents with significant viscosity contrast ($\gamma > 1$), non-Boussinesq affects will also affect flow dynamics.

In the model presented here, particle settling, cohesion, and other effects significant to turbidity current dynamics are neglected. Furthermore, the flow is assumed to be Boussinesq. However, in the three regimes identified we can infer the effect a viscosity contrast on the turbidity current at low ($c \leq 0.04$), intermediate ($c \sim 0.18$), and high ($c \gg 0.18$) particle concentrations. In the low concentration regime, $\gamma \ll 1$, turbidity currents exhibit similar viscosity to the surrounding fluid, and therefore, the effect of the viscosity contrast on the flow dynamics is minimal. In the intermediate regime of concentrations $c \sim 0.18$, the excess viscosity ratio $\gamma \sim 1$. This will reduce the rates of mixing with the ambient, decrease the propagation speed, and increase the amount of energy transferred between potential and kinetic energy. The reduced mixing rates help preserve the concentration, and crucially, the density and viscosity contrast to the ambient. For flows that are not confined to a lock-exchange domain, but instead flow down slope, a pseudo-steady supply of potential energy exists that can be continuously converted into kinetic energy and lead to turbidity currents can become self-sustaining or self-accelerating.[78] The additional transfer to kinetic energy and reduction in ambient mixing rates, when compared to low-concentration flows, enhances the flows potential to become self-sustaining. To accurately capture turbidity current dynamics at intermediate concentrations, it is not sufficient to capture the density stratification, and particle settling and resuspension and the viscosity stratification also need to be modeled.

At high concentrations ($c \gg 0.18$, $\gamma \gg 1$), viscous dissipation dominates and a further reduction in mixing with the ambient is

observed. Further, the flows propagate faster. Turbidity currents at this concentration will exhibit strong non-Boussinesq effects, which also leads to increased dissipation and propagation speed. The increased dissipation may make it impossible enough to travel great distances at the initial concentration. Further, the reduction in mixing rates reduces the flows ability to transform into a lower concentration flow. The combination of these effects suggests why some turbidity currents have long run-out lengths and can become self-sustaining, whereas some have relatively short run-out lengths. Initial composition is known to be a key control on this.[94] Our results indicate that a viscosity stratification could enhance or reduce the flows ability to travel long distances. This is likely to be enhanced by non-Newtonian properties that can arise within turbidity currents, for example, with the presence of clay.

Resolving the full structure of these flows is difficult. However, current models neglect viscosity contrast, which have affect flow dynamics as concentration increases. Most numerical studies of turbidity current dynamics assume a low particle concentration so that viscosity variations can be neglected and the Boussinesq approximation motivated (e.g., Nasr-Azadani and Meiburg,[84] Francisco *et al.*,[95] and Espath *et al.*[96]). The work presented here motivates this assumption up to low concentrations of ∼4% in terms of a viscosity stratification. However, increasing the particle concentration above $c = 0.04$ increases the excess viscosity contrast toward $\gamma \sim 1$. As the γ approaches this regime, it changes the flow dynamics as discussed earlier and the assumption breaks down. Some numerical models of turbidity currents or sedimentary flows do use a variable viscosity based on a suspension of rigid spheres (e.g., Zio *et al.*[90] and Yu *et al.*[97,98]). Zio *et al.*[90] study various viscosity models for the suspension of rigid spheres, but use a residual-based variational multiscale method, which like LES, does not resolve small scales of motion within the flow and instead models them in terms of large-scale flow properties. As such, the small-scale interface mixing dynamics are unlikely to be captured accurately. Yu *et al.*[97,98] study fine sediment transport in the bottom boundary layer with either fixed channel flow or imposed oscillatory flow, respectively, but do not extend their analysis to gravity-driven flows.

In this study, the less dense fluid 1 has fixed viscosity and the denser fluid 2 a varying viscosity. A linear mixing relationship that minimizes the maximum viscosity gradient across the interface was assumed, which is a control on the accuracy of two similar finite-element schemes.[55] However, mixing laws are often more complex. The empirical relationship determined by Cheng[83] assumes an exponential relationship between viscosity and concentration of glycerol/water mixtures. Similarly, the relationship between viscosity and concentration of a turbidity current is only linear at low concentrations.[89] Both of these profiles increase the maximum viscosity gradient for a fixed concentration profile, which may lead to an increased reduction in mixing and an enhanced interface stabilization. Further study could provide insight into the cause of the behavior observed here in the three regimes, that is, whether the viscosity contrast over the entire domain or the localized maximum viscosity gradient is the control. Furthermore, our study was restricted to fixed fluid 1 Reynolds number $Re_1 = 10^3$. Future studies investigating whether the regimes observed here are present at larger or smaller Re_1 or comparison to other equal-viscosity cases (e.g., $Re_1 = Re_2 = 500$) would provide further insight into density- and viscosity-stratified flows.

V. CONCLUSIONS

This paper explored the Boussinesq lock-exchange problem with a variable viscosity for the denser fluid over transitional to moderate Reynolds numbers. The ambient or fluid 1 Reynolds number Re_1 was fixed at 10^3. The mixture viscosity was imposed as a linear relationship of fluid 2 concentration ϕ with the fluid 2 viscosity excess viscosity ratio γ varying between 0 and 10. This linear relationship and the simple choice of domain and boundary conditions enabled the study of excess viscosity ratios γ over two orders of magnitude. The spectral element solver NEK5000 was used to conduct direct numerical simulation of the governing Navier–Stokes and advection–diffusion equation.

Three regimes depending on the excess viscosity ratio γ were identified: When the excess viscosity ratio is small, $\gamma \ll 1$, similar results are produced to those obtained for the equal-viscosity case ($\gamma = 0$). Increasing the excess viscosity ratio γ of the denser fluid reduces the rate of interface-scale mixing that occurs within the flow, which leads to a reduction in the rate of global mixing roughly one sloshing period later. Decreasing the interface-scale mixing enhances the ability of the flow to transfer energy between kinetic and potential energy. For intermediate excess viscosity ratios, $\gamma \sim 1$, the enhanced ability to transfer energy is more significant than the additional viscous dissipation in the denser fluid. Therefore, the extremal values of kinetic and potential energy for $\gamma \sim 1$ are larger for $t > 6$. However, increasing the excess viscosity above $\gamma = 2$ reduces these extrema compared with the equal-viscosity case as the rate of viscous diffusion increases. When the excess viscosity ratio is large $\gamma \gg 1$, viscous dissipation is significantly larger, which removes a significant amount of energy from the flow and further inhibits mixing. Finally, for $\gamma \sim 1$, the sloshing period decreases and increases for $\gamma \gg 1$, compared to an equal-viscosity case. Critically for modeling of geophysical density-driven flows, neglecting viscosity stratification is only a reasonable approximation in the $\gamma \ll 1$ regime. When $\gamma \sim 1$, the viscosity stratification significantly affects the flow dynamics, such as the run-out distances and flow speed, which may be more prevalent for unconfined or partially confined scenarios.

ACKNOWLEDGMENTS

P.A.A. would like to acknowledge EPSRC for providing funding for this work through the Centre for Doctoral Training in Fluid Dynamics (Grant No. EP/L01615X/1) and through the Turbidites Research Group: Aker BP; ConocoPhillips; Oxy; Murphy Oil Corporation; OMV; Harbour Energy; and CNOOC. This work was undertaken on ARC3, part of the High Performance Computing facilities at the University of Leeds, UK. We thank the anonymous referees for the constructive comments that substantially improved the quality of this manuscript.

AUTHOR DECLARATIONS

Conflict of Interest

The authors have no conflicts to disclose.

Author Contributions

Paul Andrew Allen: Conceptualization (lead); Data curation (lead); Formal analysis (lead); Investigation (lead); Methodology (lead);

Project administration (lead); Resources (lead); Software (lead); Validation (lead); Visualization (lead); Writing – original draft (lead); Writing – review & editing (equal). **Robert M Dorrell:** Supervision (equal); Writing – review & editing (equal). **Oliver Harlen:** Supervision (equal); Writing – review & editing (equal). **Robert E Thomas:** Supervision (equal); Writing – original draft (equal). **William D McCaffrey:** Supervision (equal); Writing – review & editing (equal).

DATA AVAILABILITY

The data that support the findings of this study are available from the corresponding author upon reasonable request.

APPENDIX A: DIFFUSIVE CONTRIBUTION TO MIXING

Diffusion of the concentration will slowly mix the fluid at a rate that depends on the inverse of the Péclet number $1/Pe = 1/Re_1Sc = D_m/HU$, which is independent of fluid 2 concentration ϕ. No diffusive mixing occurs, and the fluids are immiscible in the limit $Sc_1 \to \infty$. However, as discussed earlier, to accurately resolve the solution at large Schmidt numbers, increased computational resources are required. Given the initial conditions used for the lock-exchange problem (9), a lower bound of pure diffusive mixing can be obtained from the system of Eqs. (3)–(6) with $\mathbf{u} = \mathbf{0}$ everywhere and the relative impact of the Schmidt number assumption assessed. With zero velocity, this reduces to the diffusion equation

$$\frac{\partial \phi}{\partial t} = \frac{1}{Re_1 Sc}\nabla^2\phi. \tag{A1}$$

A reduced one-dimensional (in the x direction) problem is considered instead of the three-dimensional solution to the diffusion equation, with the following initial conditions:

$$\phi(x,y,z,0) = \phi_0(x) = \begin{cases} 1 & \text{if} \quad x \in [-\infty, -\zeta_0], \\ \dfrac{1}{2\zeta_0}(\zeta_0 - x) & \text{if} \quad x \in [-\zeta_0, \zeta_0], \\ 0 & \text{if} \quad x \in [\zeta_0, \infty], \end{cases} \tag{A2}$$

where $2\zeta_0 = 0.01$. Boundaries at infinity replace the flow boundaries at $x = \pm 1$, which removes the slight variation in the z direction and reduces the problem to solving a one-dimensional diffusion equation

$$\frac{\partial \phi}{\partial t} = \frac{1}{Re_1 Sc}\frac{\partial^2 \phi}{\partial x^2}. \tag{A3}$$

for each fixed y and z. Further, using an infinite domain removes negligible contribution from the boundary conditions and enables the general solution to be expressed as

$$\begin{aligned} \phi(x,t) &= \int_{-\infty}^{\infty} S(x-y,t)\phi_0(y)\,\mathrm{d}y, \\ &= \int_{-\infty}^{-\zeta_0} S(x-y,t)\,\mathrm{d}y + \int_{-\zeta_0}^{\zeta_0} S(x-y,t)\frac{\zeta_0 - y}{2\zeta_0}\,\mathrm{d}y, \end{aligned} \tag{A4}$$

where

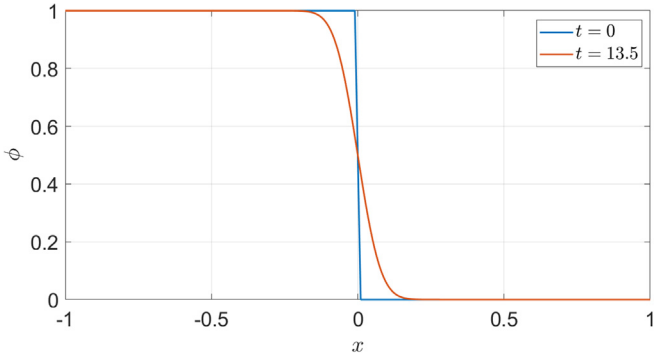

FIG. 10. Concentration profiles ϕ for a one-dimensional pure diffusion problem at $t = 0$ and $t = 13.5$. The Péclet number Pe is fixed at 7000.

$$S(x,t) = \sqrt{\frac{Re_1 Sc}{4\pi t}}\exp\left(-\frac{Re_1 Scx^2}{4t}\right) \tag{A5}$$

(see Ref. 99). These integrals are solved numerically in MATLAB[100] on a spatial grid containing 3000 points at time intervals of $\Delta t = 0.5$ up to the total integration time $T_{\text{int}} = 13.5$. The lower limit of the first integral is replaced with -10^4. These choices of spatial resolution and lower limit were checked for convergence. The concentration profile subject to diffusion at the total integration time $T_{\text{int}} = 13.5$ with $Pe = 1/(Re_1Sc) = 7000$ is presented in Fig. 10. Noticeable diffusion is observed, but localized around $x = 0$, which confirms the infinite boundary assumption.

With this profile, the three-dimensional equivalent can be reconstructed based on the initial conditions without z variation (A2). Pseudo-color plots are presented in Fig. 11 at $t = 0$ and $t = 13.5$

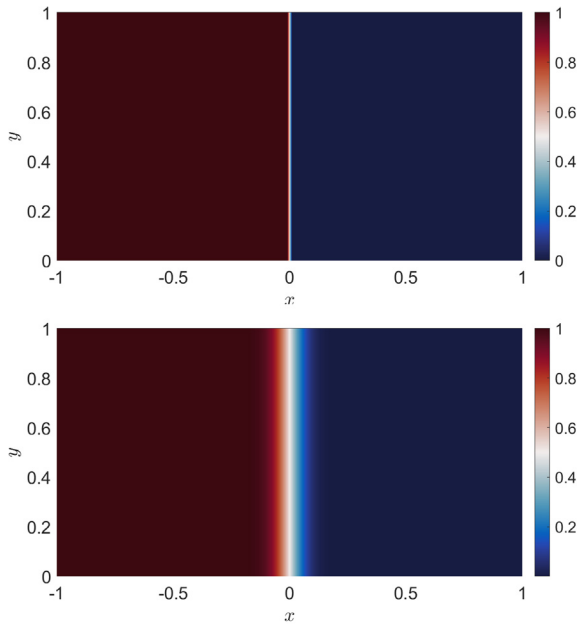

FIG. 11. Distribution of concentration ϕ in the (x, y)-plane at $t = 0$ (top) and $t = 13.5$ (bottom) for the pure diffusion problem.

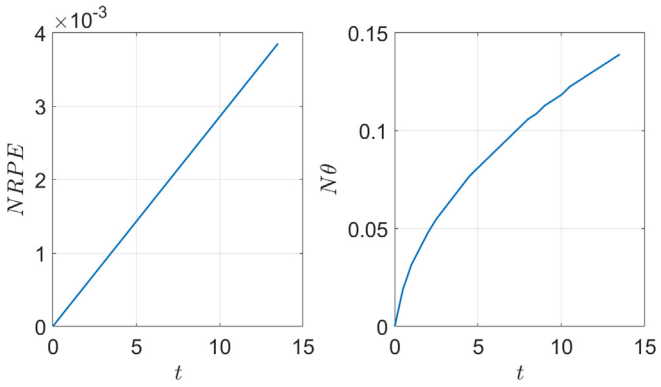

FIG. 12. Normalized residual potential energy (*NRPE*, left) and normalized θ ($N\theta$, right) over time for the pure diffusion problem.

demonstrating the change in concentration profiles arising from pure diffusion in the (x, z)-plane, in which deep red corresponding to fluid 2 ($\phi = 1$) and deep blue corresponding to fluid 1 ($\phi = 0$). Further, the change in *NRPE* and $N\theta$ over time is displayed in Fig. 12. An approximately linear increase in *NRPE* over time is observed, whereas $N\theta$ increases proportionally to $\sqrt{t}$, as locally the solution is self-similar with $\xi_0 = x/\sqrt{t}$ and has a decreasing gradient as the interface grows diffusively.

By assuming no variation in the z direction, the initial surface area of the region of the flow where $\phi(x, y, z, 0) = 0.5$ is reduced and the amount of mixing is underestimated. However, the surface area ratio ψ_0 between the curved initial conditions and the $x = 0$ plane is the same as the ratio of arc lengths or sinuosity of the z-variation

$$\psi_0 = \frac{\int_0^1 \sqrt{1 + \eta'^2}\,\mathrm{d}z}{\int_0^1 \mathrm{d}z}, \tag{A6}$$

where $\eta' = \mathrm{d}\eta/\mathrm{d}z = 0.1\cos(2\pi z)$. This integral can be reduced to a complete elliptic integral of the second kind, to which no closed form solution exists.[101] However, numerical approximations are obtained, again using MATLAB,[100] providing $\psi_0 \approx 1.024$. Thus, the error for neglecting the z-variation of the initial conditions is negligible. Further, the initial values of residual potential energy $RPE(0)$ and $\theta(0)$ are expressed in terms of ψ_0,

$$\begin{aligned} RPE(0) &= \int_0^{1/2-0.005\psi_0} y\,\mathrm{d}y \\ &\quad + \int_{1/2-0.005\psi_0}^{1/2+0.005\psi_0} \frac{1}{0.01\psi_0}(1 + 0.005\psi_0 - y)y\,\mathrm{d}y \\ &\approx 0.500\,2, \end{aligned} \tag{A7}$$

$$\theta(0) = 0.009\,8\psi_0 \approx 0.010\,04. \tag{A8}$$

These are used to compute *NRPE* and $N\theta$.

APPENDIX B: RESOLUTION

Five meshes labeled A–E are used to perform a grid independence study. The total number of nodes in the mesh n, and other mesh statistics, is presented in Table II. The number of elements in each spatial direction (N_x, N_y, N_z) are chosen to provide equal resolution in each spatial dimension, that is, $N_x = 2N_y = 2N_z$. The number of GLL points $\mathcal{N}$ is chosen to be within the optimal range of 7–15 for spectral element methods.[59] Each simulation is conducted with a Courant number $Cr = 0.1$ in the resolution study. The corresponding computation cost in terms of core hours (simulation time times the number of cores used) and the total number of cores used for each simulation are presented in Table III. The cases $\gamma = 2$ and $\gamma = 4$ were added after the initial study and not included in the grid independence study. As the resolution requirements increase with γ for the other values, it was assumed that resolved mesh for $\gamma = 10$ would be sufficient for both of these cases. All simulations were conducted on the ARC3, part of the High Performance Computing facilities at the University of Leeds, UK. Each compute node consisted of 24 Broadwell E5-2650v4 CPUs with a base frequency of 2.2 GHz. Note that the variable viscosity cases take significantly longer even when the viscosities are similar ($\gamma = 0.1$, for example) because a full discretization of the stress tensor is required.

To reduce the physical memory restraints of saving the results from each simulation, the data at each node n are exported every 0.5 dimensionless time units. The mixing and energy variables introduced in Secs. II D and II E are interpolated between these points using a piece-wise cubic spline that matches the values and gradients at the known time-steps creating a smoothed fit for the variables.

In Fig. 13, the normalized residual potential energy *NRPE* is plotted each case and each mesh used. For $\gamma = 0$ and $\gamma = 0.1$,

TABLE II. Characteristics of the five meshes. The number of elements in each spatial direction (x, y, z) is (N_x, N_y, N_z). The total number of elements in in the domain is $\mathcal{E} = N_x N_y N_z$. Each element contains $\mathcal{N}$ GLL points in each spatial direction giving the total number of nodes $n = \mathcal{E}\mathcal{N}^3$.

Mesh	N_x	N_y	N_z	E	$\mathcal{N}$	n
A	32	16	16	8 192	8	4 194 304
B	48	24	24	27 648	9	20 155 392
C	60	30	30	54 000	9	39 366 000
D	72	36	36	93 312	9	68 024 448
E	84	42	42	148 176	9	108 020 304

TABLE III. Computational time in core hours (number of computational cores times the clock time) for each case and mesh. The number of cores used for each simulation is shown in brackets. Dashes indicate that a lower resolution mesh was deemed sufficiently resolved and hence not conducted for that mesh.

Mesh	$\gamma = 0$	$\gamma = 0.1$	$\gamma = 1$	$\gamma = 10$
A	213 (48)	424 (48)	394 (48)	463 (48)
B	2361 (96)	4 303 (120)	3 999 (120)	3 592 (120)
C	5890 (192)	14 244 (216)	10 700 (216)	9 118 (216)
D	⋯	⋯	⋯	20 152 (432)
E	⋯	⋯	⋯	37 829 (480)

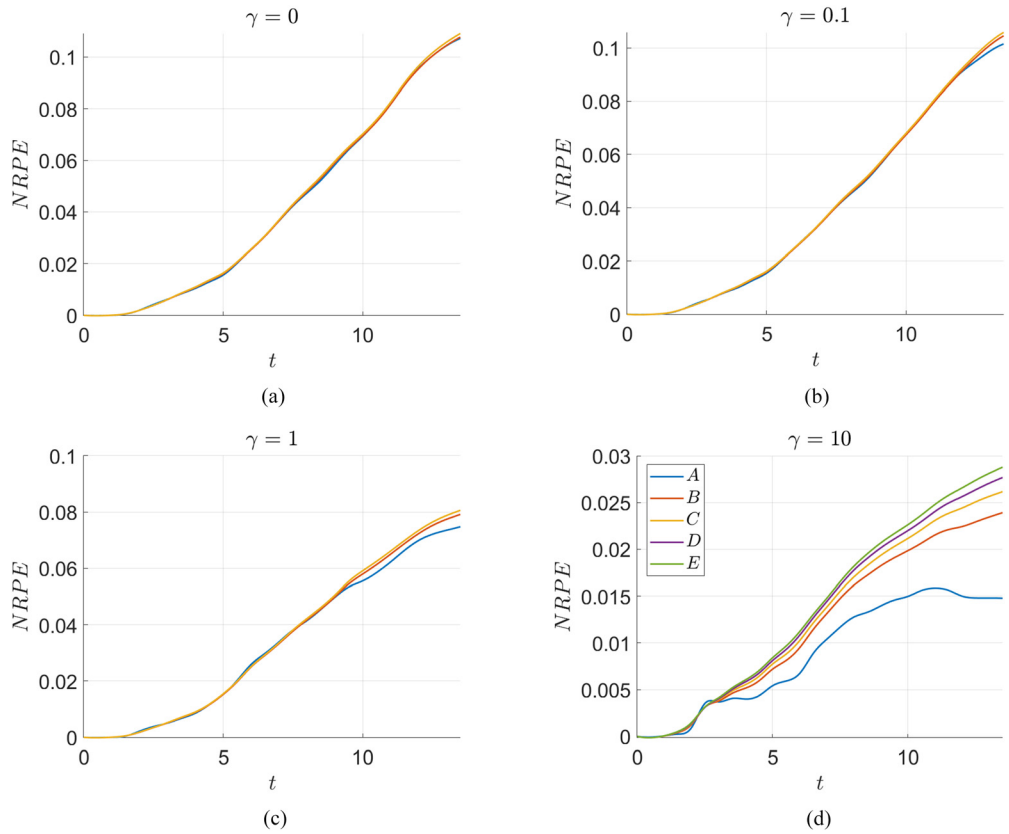

FIG. 13. Normalized residual potential energy *NRPE* against time for the meshes considered for each case: (a) $\gamma = 0$, (b) $\gamma = 0.1$, (c) $\gamma = 1$, and (d) $\gamma = 10$.

similar results are obtained for all the meshes considered indicating that the meshes are sufficiently resolved. As the viscosity difference between the layers increases ($\gamma = 1$ and $\gamma = 10$), higher resolution is required to produce a mesh-independent solution. In particular, the *NRPE* on mesh *B* is not sufficient for $\gamma = 1$, as it deviates after approximately $t = 9$. Further, a distinct difference between the *NRPE* for all five meshes for $\gamma = 10$ is observed. A higher resolution mesh would be required for $\gamma = 10$ to confirm that the mesh *E*,

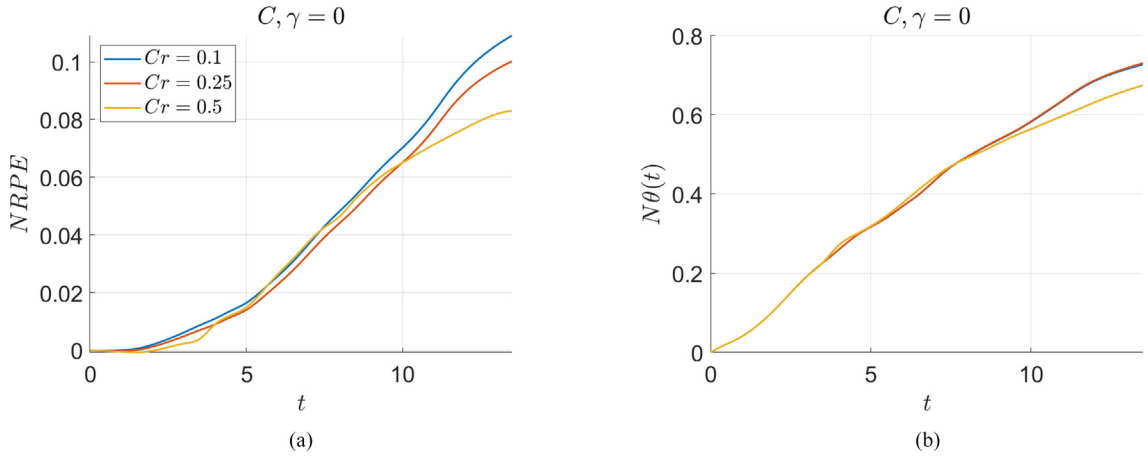

FIG. 14. Normalized residual potential energy *NRPE* (a) and normalized volume fraction of mixed fluid $N\theta$ (b) against time for mesh *C* and $\gamma = 0$ at different Courant numbers.

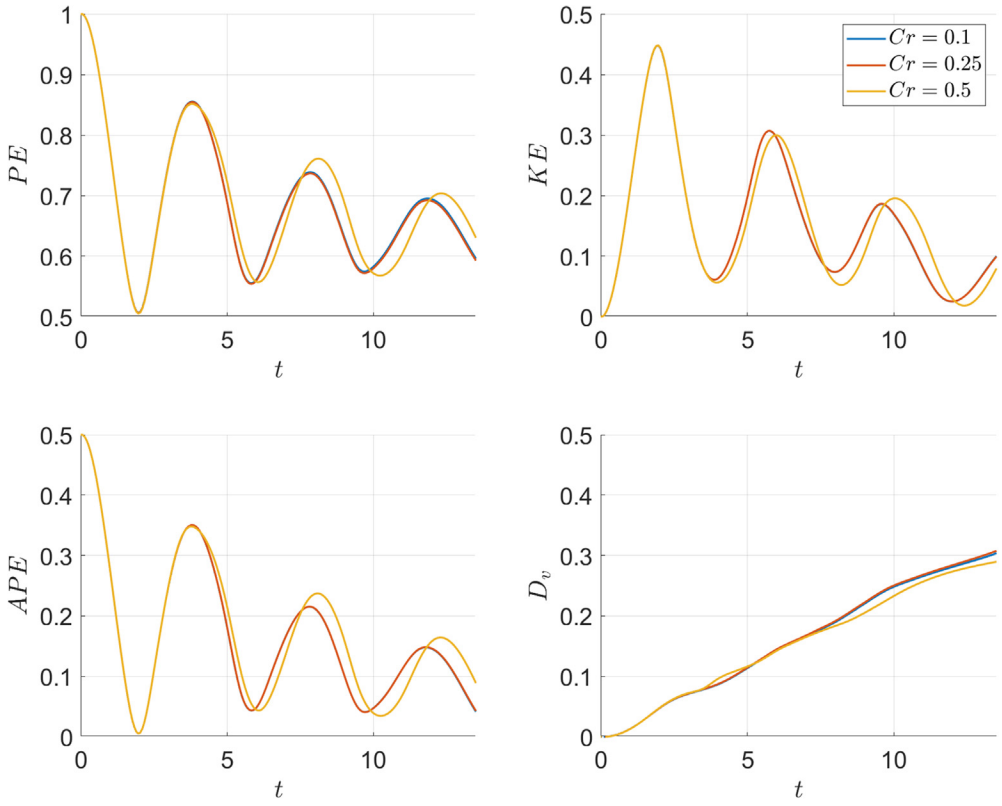

FIG. 15. Potential energy (*PE*), kinetic energy (*KE*), available potential energy (*APE*), and dissipated energy D_v for $\gamma = 0$ on mesh *C* with Courant numbers of 0.1, 0.25, and 0.5.

$\gamma = 10$ solution is completely resolved. Apart from the solution obtained using the coarsest mesh, *A*, curves of normalized mixing fraction $N\theta(t)$, potential energy *PE*, kinetic energy *KE*, available potential energy *APE*, and dissipated energy D_v are coincident.

Finally, the $\gamma = 0$ on mesh *C*, normalized residual potential energy *NRPE*, and normalized theta $N\theta$ are plotted for three different Courant numbers *Cr* (0.5, 0.25, 0.1) in Fig. 14. Decreasing the Courant number decreases the time step used, and similarly to decreasing the spatial resolution, both *NRPE* and $N\theta$ produce similar results for $Cr = 0.1$ and $Cr = 0.25$. Although the *NRPE* is not coincident for $Cr = 0.1$ and $Cr = 0.25$, it is for the remaining energy distributions, Fig. 15. Thus, a Courant number of 0.1 is sufficient for all simulations.

REFERENCES

[1]H. E. Huppert, "Gravity currents: A personal perspective," J. Fluid Mech. **554**, 299 (2006).
[2]J. Simpson, *Gravity Currents: In the Environment and the Laboratory* (Cambridge University Press, 1999).
[3]C. G. Johnson and A. J. Hogg, "Entraining gravity currents," J. Fluid Mech. **731**, 477–508 (2013).
[4]D. P. Hoult, "Oil spreading on the sea," Annu. Rev. Fluid Mech. **4**, 341–368 (1972).
[5]H. E. Huppert and J. E. Simpson, "The slumping of gravity currents," J. Fluid Mech. **99**, 785–799 (1980).
[6]H. E. Huppert, "The propagation of two-dimensional and axisymmetric viscous gravity currents over a rigid horizontal surface," J. Fluid Mech. **121**, 43–58 (1982).
[7]J. O. Shin, S. B. Dalziel, and P. F. Linden, "Gravity currents produced by lock exchange," J. Fluid Mech. **521**, 1–34 (2004).
[8]R. J. Lowe, J. W. Rottman, and P. F. Linden, "The non-Boussinesq lock-exchange problem. I. Theory and experiments," J. Fluid Mech. **537**, 101–124 (2005).
[9]M. Ungarish, *An Introduction to Gravity Currents and Intrusions* (Chapman and Hall/CRC, 2009).
[10]W. Peltier and C. Caulfield, "Mixing efficiency in stratified shear flows," Annu. Rev. Fluid Mech. **35**, 135–167 (2003).
[11]B. R. Morton, G. I. Taylor, and J. S. Turner, "Turbulent gravitational convection from maintained and instantaneous sources," Proc. R. Soc. London, Ser. A **234**, 1–23 (1956).
[12]J. S. Turner, "Turbulent entrainment: The development of the entrainment assumption, and its application to geophysical flows," J. Fluid Mech. **173**, 431–471 (1986).
[13]T. Bonometti and S. Balachandar, "Effect of Schmidt number on the structure and propagation of density currents," Theor. Comput. Fluid Dyn. **22**, 341 (2008).
[14]F. Necker, C. Härtel, L. Kleiser, and E. Meiburg, "Mixing and dissipation in particle-driven gravity currents," J. Fluid Mech. **545**, 339–372 (2005).
[15]V. K. Birman, J. E. Martin, and E. Meiburg, "The non-Boussinesq lock-exchange problem. part 2. high-resolution simulations," J. Fluid Mech. **537**, 125–144 (2005).
[16]E. Meiburg and B. Kneller, "Turbidity currents and their deposits," Annu. Rev. Fluid Mech. **42**, 135–156 (2010).
[17]E. Gonzalez-Juez, E. Meiburg, and G. Constantinescu, "Gravity currents impinging on bottom-mounted square cylinders: Flow fields and associated forces," J. Fluid Mech. **631**, 65–102 (2009).
[18]B. Barley, "Deepwater problems around the world," Leading Edge **18**, 488–493 (1999).

[19]A. T. Dengler, P. Wilde, E. K. Noda, and W. R. Normark, "Turbidity currents generated by hurricane Iwa," Geo-Mar. Lett. **4**, 5–11 (1984).
[20]B. C. Heezen and M. Ewing, "Turbidity currents and submarine slumps, and the 1929 grand banks earthquake," Am. J. Sci. **250**, 849–873 (1952).
[21]P. Weimer, R. M. Slatt, and R. Bouroullec, *Introduction to the Petroleum Geology of Deep-Water Settings* (American Association of Petroleum Geologists, 2007), Vol. 57.
[22]P. J. Talling, D. G. Masson, E. J. Sumner, and G. Malgesini, "Subaqueous sediment density flows: Depositional processes and deposit types," Sedimentology **59**, 1937–2003 (2012).
[23]M. Felix and J. Peakall, "Transformation of debris flows into turbidity currents: Mechanisms inferred from laboratory experiments," Sedimentology **53**, 107–123 (2006).
[24]J. Stickel and R. Powell, "Fluid mechanics and rheology of dense suspensions," Annu. Rev. Fluid Mech. **37**, 129–149 (2005).
[25]E. Meiburg, S. Radhakrishnan, and M. M. Nasr-Azadani, "Modeling gravity and turbidity currents: Computational approaches and challenges," Appl. Mech. Rev. **67**, 040802 (2015).
[26]E. Sumner, P. Talling, and L. Amy, "Deposits of flows transitional between turbidity current and debris flow," Geology **37**, 991–994 (2009).
[27]P. H. Kuenen and C. I. Migliorini, "Turbidity currents as a cause of graded bedding," J. Geol. **58**, 91–127 (1950).
[28]L. Chiapponi, M. Ungarish, D. Petrolo, V. D. Federico, and S. Longo, "Non-Boussinesq gravity currents and surface waves generated by lock release in a circular-section channel: Theoretical and experimental investigation," J. Fluid Mech. **869**, 610–633 (2019).
[29]M. Maggi, C. Adduce, and M. Negretti, "Lock-release gravity currents propagating over roughness elements," Environ. Fluid Mech. **22**, 383–320 (2022).
[30]R. Wilson, H. Friedrich, and C. Stevens, "Quantifying propagation characteristics of unconfined turbidity currents interacting with an obstacle within the slumping regime," J. Hydraul. Res. **57**, 498–516 (2019).
[31]M. De Falco, C. Adduce, and M. Maggi, "Gravity currents interacting with a bottom triangular obstacle and implications on entrainment," Adv. Water Resour. **154**, 103967 (2021).
[32]C. Adduce, M. Maggi, and M. De Falco, "Non-intrusive density measurements in gravity currents interacting with an obstacle," Acta Geophys. (published online 2022).
[33]R. Wilson, H. Friedrich, and C. Stevens, "Image thresholding process for combining photometry with intrusive flow instruments," J. Hydraul. Res. **56**, 282–290 (2018).
[34]V. Ho, R. Dorrell, G. Keevil, A. Burns, and W. McCaffrey, "Pulse propagation in turbidity currents," Sedimentology **65**, 620–637 (2018).
[35]V. Ho, R. Dorrell, G. Keevil, A. Burns, and W. McCaffrey, "Scaling analysis of multipulsed turbidity current evolution with application to turbidite interpretation," J. Geophys. Res.: Oceans **123**, 3668–3684, https://doi.org/10.1029/2017JC013463 (2018).
[36]V. Ho, R. Dorrell, G. Keevil, R. Thomas, A. Burns, J. Baas, and W. McCaffrey, "Dynamics and deposition of sediment-bearing multi-pulsed flows and geological implication," J. Sediment. Res. **89**, 1127–1139 (2019).
[37]J. A. Fay, "Physical processes in the spread of oil on a water surface," Int. Oil Spill Conf. Proc. **1971**, 463–467.
[38]A. J. Hogg, "Lock-release gravity currents and dam-break flows," J. Fluid Mech. **569**, 61–87 (2006).
[39]R. M. Dorrell, S. E. Darby, J. Peakall, E. J. Sumner, D. R. Parsons, and R. B. Wynn, "The critical role of stratification in submarine channels: Implications for channelization and long runout of flows," J. Geophys. Res.: Oceans **119**, 2620–2641, https://doi.org/10.1002/2014JC009807 (2014).
[40]P. Allen, R. Dorrell, O. Harlen, R. Thomas, and W. McCaffrey, "Pulse propagation in gravity currents," Phys. Fluids **32**, 016603 (2020).
[41]A. Kassem and J. Imran, "Three-dimensional modeling of density current. II. Flow in sinuous confined and unconfined channels," J. Hydraul. Res. **42**, 591–602 (2004).
[42]J. Imran, A. Kassem, and S. M. Khan, "Three-dimensional modeling of density current. I. Flow in straight confined and unconfined channels," J. Hydraul. Res. **42**, 578–590 (2004).
[43]H. Burchard, F. Janssen, K. Bolding, L. Umlauf, and H. Rennau, "Model simulations of dense bottom currents in the Western Baltic Sea," Cont. Shelf Res. **29**, 205–220 (2009).
[44]P. Sagaut, *Large Eddy Simulation for Incompressible Flows: An Introduction* (Springer Science & Business Media, 2006).
[45]T. M. Özgökmen, T. Iliescu, and P. F. Fischer, "Reynolds number dependence of mixing in a lock-exchange system from direct numerical and large eddy simulations," Ocean Modell. **30**, 190–206 (2009).
[46]C. Härtel, E. Meiburg, and F. Necker, "Analysis and direct numerical simulation of the flow at a gravity-current head. I. Flow topology and front speed for slip and no-slip boundaries," J. Fluid Mech. **418**, 189–212 (2000).
[47]C. Härtel, L. Kleiser, M. Michaud, and C. F. Stein, "A direct numerical simulation approach to the study of intrusion fronts," J. Eng. Math. **32**, 103–120 (1997).
[48]F. Necker, C. Härtel, L. Kleiser, and E. Meiburg, "High-resolution simulations of particle-driven gravity currents," Int. J. Multiphase Flow **28**, 279–300 (2002).
[49]T. M. Özgökmen, T. Iliescu, P. F. Fischer, A. Srinivasan, and J. Duan, "Large eddy simulation of stratified mixing in two-dimensional dam-break problem in a rectangular enclosed domain," Ocean Modell. **16**, 106–140 (2007).
[50]T. M. Özgökmen, T. Iliescu, and P. F. Fischer, "Large eddy simulation of stratified mixing in a three-dimensional lock-exchange system," Ocean Modell. **26**, 134–155 (2009).
[51]M. I. Cantero, S. Balachandar, M. H. García, and J. P. Ferry, "Direct numerical simulations of planar and cylindrical density currents," J. Appl. Mech. **73**, 923–930 (2006).
[52]M. I. Cantero, J. R. Lee, S. Balachandar, and M. H. Garcia, "On the front velocity of gravity currents," J. Fluid Mech. **586**, 1–39 (2007).
[53]P. F. Fischer, J. W. Lottes, S. G. Kerkemeier, *et al.*, see https://nek5000.mcs.anl.gov/ for "nek5000 web page," 2008.
[54]R. Scardovelli and S. Zaleski, "Direct numerical simulation of free-surface and interfacial flow," Annu. Rev. Fluid Mech. **31**, 567–603 (1999).
[55]L. Moresi, S. Zhong, and M. Gurnis, "The accuracy of finite element solutions of Stokes's flow with strongly varying viscosity," Phys. Earth Planet. Inter. **97**, 83–94 (1996).
[56]M. Il icak, T. M. Özgökmen, E. Özsoy, and P. F. Fischer, "Non-hydrostatic modeling of exchange flows across complex geometries," Ocean Modell. **29**, 159–175 (2009).
[57]J. Boussinesq, *Théorie de L'écoulement Tourbillonnant et Tumultueux Des Liquides Dans Les Lits Rectilignes a Grande Section* (Gauthier-Villars, 1897), Vol. 1.
[58]D. J. Tritton, *Physical Fluid Dynamics* (Springer Science & Business Media, 2012).
[59]A. T. Patera, "A spectral element method for fluid dynamics: Laminar flow in a channel expansion," J. Comput. Phys. **54**, 468–488 (1984).
[60]M. O. Deville, P. F. Fischer, E. H. Mund *et al.*, *High-Order Methods for Incompressible Fluid Flow* (Cambridge University Press, 2002), Vol. 9.
[61]A. G. Tomboulides, J. C. Y. Lee, and S. A. Orszag, "Numerical simulation of low Mach number reactive flows," J. Sci. Comput. **12**, 139–167 (1997).
[62]A. G. Tomboulides and S. A. Orzag, "A quasi-two-dimensional benchmark problem for low Mach number compressible codes," J. Comput. Phys. **146**, 691–706 (1998).
[63]D. L. Brown, "Performance of under-resolved two-dimensional incompressible flow simulations," J. Comput. Phys. **122**, 165–183 (1995).
[64]T. M. Özgökmen, P. F. Fischer, J. Duan, and T. Iliescu, "Three-dimensional turbulent bottom density currents from a high-order nonhydrostatic spectral element model," J. Phys. Oceanogr. **34**, 2006–2026 (2004).
[65]T. M. Özgökmen and P. F. Fischer, "On the role of bottom roughness in overflows," Ocean Modell. **20**, 336–361 (2008).
[66]S. Lomperski, A. Obabko, E. Merzari, P. Fischer, and W. D. Pointer, "Jet stability and wall impingement flow field in a thermal striping experiment," Int. J. Heat Mass Transfer **115**, 1125–1136 (2017).
[67]R. M. Kirby and G. E. Karniadakis, "De-aliasing on non-uniform grids: Algorithms and applications," J. Comput. Phys. **191**, 249–264 (2003).
[68]J. Ohlsson, P. Schlatter, P. F. Fischer, and D. S. Henningson, "Stabilization of the spectral-element method in turbulent flow simulations," in *Spectral and*

High Order Methods for Partial Differential Equations (Springer, 2011), pp. 449–458.
[69]A. Kraus, E. Merzari, T. Norddine, O. Marin, and S. Benhamadouche, "Direct numerical simulation of fluid flow in a 5x5 square rod bundle using nek5000," in *International Conference on Nuclear Engineering* (American Society of Mechanical Engineers, 2020), Vol. 83785, p. V003T12A036.
[70]E. Merzari, W. Pointer, and P. Fischer, "Numerical simulation and proper orthogonal decomposition of the flow in a counter-flow t-junction," J. Fluids Eng. **135**, 091304 (2013).
[71]J. Martínez, E. Merzari, M. Acton, and E. Baglietto, "Direct numerical simulation of turbulent flow inside a differentially heated composite cavity," Nucl. Technol. **206**, 266–282 (2020).
[72]E. Merzari, P. Fischer, M. Min, S. Kerkemeier, A. Obabko, D. Shaver, H. Yuan, Y. Yu, J. Martinez, L. Brockmeyer *et al.*, "Toward exascale: Overview of large eddy simulations and direct numerical simulations of nuclear reactor flows with the spectral element method in nek5000," Nucl. Technol. **206**, 1308–1324 (2020).
[73]K. B. Winters, P. N. Lombard, J. J. Riley, and E. A. D'Asaro, "Available potential energy and mixing in density-stratified fluids," J. Fluid Mech. **289**, 115–128 (1995).
[74]E. Lorenz, "Available potential energy and the maintenance of the general circulation," Tellus **7**, 157–167 (1955).
[75]Y. Tseng and J. H. Ferziger, "Mixing and available potential energy in stratified flows," Phys. Fluids **13**, 1281–1293 (2001).
[76]T. Agrawal, B. Ramesh, S. Zimmerman, J. Philip, and J. Klewicki, "Probing the high mixing efficiency events in a lock-exchange flow through simultaneous velocity and temperature measurements," Phys. Fluids **33**, 016605 (2021).
[77]P. Mukherjee and S. Balasubramanian, "Diapycnal mixing efficiency in lock-exchange gravity currents," Phys. Rev. Fluids **6**, 013801 (2021).
[78]G. Parker, Y. Fukushima, and H. Pantin, "Self-accelerating turbidity currents," J. Fluid Mech. **171**, 145–181 (1986).
[79]M. Generous, N. Qasem, B. Qureshi, and S. Zubair, "A comprehensive review of saline water correlations and data. I. Thermodynamic properties," Arabian J. Sci. Eng. **45**, 8817–8860 (2020).
[80]N. Qasem, M. Generous, B. Qureshi, and S. Zubair, "A comprehensive review of saline water correlations and data. II. Thermophysical properties," Arabian J. Sci. Eng. **46**, 1941–1939 (2021).
[81]R. Christoph, B. Schmidt, U. Steinberner, W. Dilla, and R. Karinen, "Glycerol," in *Ullmann's Encyclopedia of Industrial Chemistry* (American Cancer Society, 2006).
[82]L. Amy, A. Hogg, J. Peakall, and P. Talling, "Abrupt transitions in gravity currents," J. Geophys. Res.: Earth Surf. **110**, F03001, https://doi.org/10.1029/2004JF000197 (2005).
[83]N. S. Cheng, "Formula for the viscosity of a glycerol–water mixture," Ind. Eng. Chem. Res. **47**, 3285–3288 (2008).
[84]M. M. Nasr-Azadani and E. Meiburg, "Turbins: An immersed boundary, Navier–Stokes code for the simulation of gravity and turbidity currents interacting with complex topographies," Comput. Fluids **45**, 14–28 (2011).
[85]A. Ooi, N. Zgheib, and S. Balachandar, "Direct numerical simulation of three-dimensional gravity current on a uniform slope," Procedia Eng. **126**, 372–376 (2015).
[86]J. Penney and M. Stastna, "Direct numerical simulation of double-diffusive gravity currents," Phys. Fluids **28**, 086602 (2016).
[87]R. Ouillon, C. Kakoutas, E. Meiburg, and T. Peacock, "Gravity currents from moving sources," J. Fluid Mech. **924**, A43 (2021).
[88]K. Steenhauer, T. Tokyay, and G. Constantinescu, "Dynamics and structure of planar gravity currents propagating down an inclined surface," Phys. Fluids **29**, 036604 (2017).
[89]H. Shewan and J. Stokes, "Analytically predicting the viscosity of hard sphere suspensions from the particle size distribution," J. Non-Newtonian Fluid Mech. **222**, 72–81 (2015).
[90]S. Zio, H. da Costa, G. Guerra, P. Paraizo, J. Camata, R. Elias, A. Coutinho, and F. Rochinha, "Bayesian assessment of uncertainty in viscosity closure models for turbidity currents computations," Comput. Methods Appl. Mech. Eng. **342**, 653–673 (2018).
[91]A. Einstein, "A new determination of the molecular dimension," Ann. Phys. **34**, 591–592 (1911).
[92]S. Maron and P. Pierce, "Application of Ree-Eyring generalized flow theory to suspensions of spherical particles," J. Colloid Sci. **11**, 80–95 (1956).
[93]I. Krieger and T. Dougherty, "A mechanism for non-Newtonian flow in suspensions of rigid spheres," Trans. Soc. Rheol. **3**, 137–152 (1959).
[94]P. Talling, J. Peakall, R. Sparks, C. Cofaigh, J. Dowdeswell, M. Felix, R. Wynn, J. Baas, A. Hogg, D. Masson *et al.*, "Experimental constraints on shear mixing rates and processes: Implications for the dilution of submarine debris flows," Geol. Soc., London, Spec. Publ. **203**, 89–103 (2002).
[95]E. Francisco, L. Espath, and J. Silvestrini, "Direct numerical simulation of bidisperse particle-laden gravity currents in the channel configuration," Appl. Math. Modell. **49**, 739–752 (2017).
[96]L. Espath, L. Pinto, S. Laizet, and J. Silvestrini, "High-fidelity simulations of the lobe-and-cleft structures and the deposition map in particle-driven gravity currents," Phys. Fluids **27**, 056604 (2015).
[97]X. Yu, T. Hsu, and S. Balachandar, "A spectral-like turbulence-resolving scheme for fine sediment transport in the bottom boundary layer," Comput. Geosci. **61**, 11–22 (2013).
[98]X. Yu, C. Ozdemir, T. Hsu, and S. Balachandar, "Numerical investigation of turbulence modulation by sediment-induced stratification and enhanced viscosity in oscillatory flows," J. Waterway, Port, Coastal, Ocean Eng. **140**, 160–172 (2014).
[99]L. Evans, *Partial Different Equations* (American Mathematical Society, 2010).
[100]MATLAB 9.4.0, The MathWorks Inc., Natick, MA, 2018.
[101]B. C. Carlson, "Numerical computation of real or complex elliptic integrals," Numer. Algorithms **10**, 13–26 (1995).